# MODELING OF CRACK TIP

# HIGH INERTIA ZONE

# IN DYNAMIC BRITTLE FRACTURE

A Dissertation

by

SHANKAR KAREDLA-RAVI

Submitted to the Office of Graduate Studies of
Texas A&M University
in partial fulfillment of the requirements for the degree of

DOCTOR OF PHILOSOPHY

May 2006

Major Subject: Mechanical Engineering

# MODELING OF CRACK TIP

# HIGH INERTIA ZONE

# IN DYNAMIC BRITTLE FRACTURE

A Dissertation

by

SHANKAR KAREDLA-RAVI

Submitted to the Office of Graduate Studies of
Texas A&M University
in partial fulfillment of the requirements for the degree of

DOCTOR OF PHILOSOPHY

Approved by:

| | |
|---|---|
| Chair of Committee, | J. N. Reddy |
| Committee Members, | Jay R. Walton |
| | Vikram K. Kinra |
| | Harry Hogan |
| Head of Department, | Dennis L. O'Neal |

May 2006

Major Subject: Mechanical Engineering

## ABSTRACT

Modeling of Crack Tip High
Inertia Zone in Dynamic Brittle Fracture. (May 2006)
Shankar Karedla-Ravi, B.S., Indian Institute of Technology-Madras;
M.S., University of Missouri-Rolla
Chair of Advisory Committee: Dr. J. N. Reddy

A phenomenological cohesive term is proposed and added to an existing cohesive constitutive law (by Roy and Dodds) to model the crack tip high inertia region proposed by Gao. The new term is attributed to fracture mechanisms that result in high energy dissipation around the crack tip and is assumed to be a function of external energy per volume input into the system. Finite element analysis is performed on PMMA with constant velocity boundary conditions and mesh discretization based on the work of Xu and Needleman. The cohesive model with the proposed dissipative term is only applied in the high inertia zone i.e., to cohesive elements very close to the crack tip and the traditional Roy and Dodds model is applied on cohesive elements in the rest of the domain. It was observed that crack propagated in three phases with a speed of $0.35c_R$ before branching, which are in good agreement with experimental observations. Thus, modeling of high inertia zone is one of the key aspects to understanding brittle fracture.

# DEDICATION

To my mother

## ACKNOWLEDGMENTS

I would like to thank my committee chair, Dr. J. N. Reddy, and my committee members, Dr. Walton, Dr. Hogan and Dr. Kinra for their guidance and support throughout the course of this research.

Thanks also to my colleagues at the Advanced Computational Mechanics Lab, my friends and various organizations/departments at Texas A&M University especially, AID-TAMU, Art of Living A&M Group, Texas A&M Astronomical Observatory, Student Activities etc., for making my time here a great experience.

Finally, I would like to express my sincere gratitude to my parents, grandparents, sister and brother-in-law and friends across the globe for continuous support and encouragement.

# TABLE OF CONTENTS

# LIST OF FIGURES

Page

Page

# LIST OF TABLES

Page

# 1. INTRODUCTION

## 1.1. Overview

With the growth of science and technology, engineering materials are being pushed to new limits. For the safety of men and material supported by structures built with engineering materials, the study of various failure mechanisms of these materials is of utmost importance. Materials fail by various mechanisms like carrying excess loads, stress concentrations, oscillations, fatigue, fracture, creep etc.

Engineering materials as a result of production and manufacturing processes contain flaws. These flaws may lead to initiation and propagation of cracks under various loading conditions. As all failure modes, failure by fracture has been a subject of great interests to engineers for over a century. Fracture under statically applied loads or under a specified displacement is termed as quasi-static crack growth.

In addition to quasi-static crack growth, dynamic crack growth in brittle and ductile materials has also been subjected to intense study. With growing importance of impact and crash proof materials, understanding the mechanism for dynamic failure in these materials will help in better design of various structures. Early continuum based developments in dynamic fracture models, termed as elastodynamic fracture mechanics, were an extension of static crack principles.

Fracture theories based on continuum mechanics resulted in square root singular crack tip stress field. This stress field for Mode-I fracture is given in terms of the dynamic stress intensity factor $K_I(t)$ as (Freund, 1990)

$$\sigma_{ij} = \frac{K_I(t)}{\sqrt{2\pi r}} \Sigma_{ij}^{I}(\theta, v) \tag{1.1}$$

---

This thesis follows the style of *International Journal of Fracture*.

The functions $\Sigma_{ij}^{I}(\theta, v)$ represent angular variations of stresses at the instantaneous crack speed $v$ and are

$$\Sigma_{11}^{I} = \frac{1}{D}\left\{\left(1+\alpha_s^2\right)\left(1+2\alpha_d^2-\alpha_s^2\right)\frac{\cos\theta_d/2}{\sqrt{\gamma_d}} - 4\alpha_s\alpha_d\frac{\cos\theta_s/2}{\sqrt{\gamma_s}}\right\}$$
$$\Sigma_{12}^{I} = \frac{2\alpha_s\left(1+\alpha_s^2\right)}{D}\left\{\frac{\sin\theta_d/2}{\sqrt{\gamma_d}} - \frac{\sin\theta_s/2}{\sqrt{\gamma_s}}\right\} \qquad (1.2)$$
$$\Sigma_{22}^{I} = -\frac{1}{D}\left\{\left(1+\alpha_s^2\right)^2\frac{\cos\theta_d/2}{\sqrt{\gamma_d}} - 4\alpha_s\alpha_d\frac{\cos\theta_s/2}{\sqrt{\gamma_s}}\right\}$$

where

$$D = 4\alpha_d\alpha_s - (1+\alpha_s^2)^2$$
$$\gamma_d = \sqrt{1-\left(v\sin\theta/c_d\right)^2} \qquad \tan\theta_d = \alpha_d\tan\theta \qquad (1.3)$$
$$\gamma_s = \sqrt{1-\left(v\sin\theta/c_s\right)^2} \qquad \tan\theta_s = \alpha_s\tan\theta$$

and

$$\alpha_s = \sqrt{1-v^2/c_s^2} \qquad \alpha_d = \sqrt{1-v^2/c_d^2} \qquad (1.4)$$

$c_s$ and $c_d$ are the shear and longitudinal wave speeds.

The hoop stress is maximum at $\theta = 0^o$ for low crack velocities. However, then the velocity exceeds $0.6c_s$ the hoop stress develops maximum around $\theta = 60^o$. Yoffe (1951) first showed the significance of the stress modification in front of the crack tip to crack branching phenomenon.

The energy release rate G, which for a linear elastic material is defined as the rate of change of potential energy with crack area is given as

$$G = \frac{A_I(v)K_I^2}{E'} \tag{1.5}$$

where

$$A_I(v) = \frac{v^2\alpha_d}{(1-\nu)c_s^2 D} \tag{1.6}$$

and

$$E' = E \qquad \text{(plane stress)}$$
$$E' = \frac{E}{1-\nu^2} \qquad \text{(plane strain)} \tag{1.7}$$

$A_I$ depends on crack velocity and material properties but are independent of the applied loading and configuration of the body, hence also considered an universal function just as $\Sigma_{ij}^I(\theta, v)$.

$A_I$ = O[$(c_R\text{-}v)^{-1}$] (read 'O' as 'order of') and D → 0 as v → $c_R$. Thus, Equation 1.5 predicts that the maximum speed that a crack can attain is $c_R$, the Rayleigh surface wave speed.

Elastodynamics predicts experimental results quit well in material which undergo failure under large plastic deformation. Hence, dynamic fracture of ductile materials is well established through elastodynamics.

However, the study of brittle fracture under high dynamic loading conditions is an on going process. Extensive research has been done in this field since early last century. There is a wealth of experimental data and, both computational and analytic work available which provide a good understanding for the dynamic fast crack growth in

isotropic brittle materials. However, there are few unexplained failure phenomenon that have been observed in various experiments. Most for the experiments in this field of research have been performed on organic glassy polymers like polymethylmethacrylate (PMMA), polystyrene (PS), Homalite-100 etc., which are macroscopically brittle under these high loading conditions. In these materials, it was observed that the macroscopic crack speed never approached Rayleigh wave speed as predicted by elastodynamics. Change in material structure, while undergoing fracture from “mirror” to “mist” to “hackle”, formation of parabolic marking, surface roughness, high crack tip temperature, instability in crack speed, velocity discontinuity, microbranching, low branching angle are some of the phenomenon observed in experiments that are yet to be completely and satisfactorily explained.

### 1.2. Literature Review

As stated above, there is wealth of information in this field. Thus, the literature review is divided into experimental, computational and analytical work review.

#### 1.2.1. Review of Experimental Work

The most common of organic material is the easily available, PMMA. Carlsson et al. (1973) studied fast fracture using single edge notch specimens made of PMMA under three different prescribed displacement conditions. Crack speed was measured using the electric impedance method. In this method, thin electrically conducting strips are applied and an alternating current is passed through the test specimen which is a source of impedance. Due to crack opening during propagation, the conducting strips breaks, affecting the total impedance. By continuously measuring the resistance offered by the specimen during crack propagation the instantaneous crack tip position can be determined from which the crack speed is calculated. In the experiments, they observed steady crack propagation followed by unstable propagation with crack velocity oscillations, but the velocity was constant in an average sense. They also observed on the surface rough river patterns, parabolic markings and macrocrack branching during

unstable propagation. The density of these markings increased linearly with crack velocity. The same trend was noticed for various loading conditions indicating the same failure mechanism.

Crack initiation and arrest criteria with critical stress intensity factor as the main parameter was studied by Ravi-Chandar and Knauss (1984a). In their work, discontinuous transition of crack velocity from near stationary to steady-state motion was observed. Characteristic surface appearances referred to as “mirror”, “mist” and “hackle” were also observed by Ravi-Chandar and Knauss (1984b). As the crack tip heads from steady to unsteady propagation, the surface structure changes from mirror to mist and then to a hackle appearance. The stress intensity increased from one zone to the other. The intense stress intensity at the crack tip induces nucleation of flaw in the structure. These flaws coalesce to form microcracks and microbranches. The parabolic appearances noticed by Carlson et al. (1973) were also observed here in the mist and hackle region. The interaction of microcracks with the main crack front is proposed to be the mechanism for conic and parabolic markings.

Ravi-Chandar and Knauss (1984c) also proposed a microcrack based branching model. In the model they put forth that branching was not because of critical stress intensity but to be a result of continuous interaction of microcracks and microbranches with the main crack front. They also observed that there was no significant change in the crack velocity before and after branching. In addition, the macroscopic crack speed remained unaffected, above a critical limit, irrespective of changes in stress intensity factor and stress wave interactions.

A detailed investigation on the interaction of propagating cracks with stress waves was performed by Ravi-Chandar and Knauss (1984d) in their final of series of four papers. In these experiments they observed that a stress wave can induce branching or affected a change in the direction of crack propagation, but stress wave interaction is not a necessary criterion for branching.

Resistance measurement technique was used to obtain velocity resolution of 25-30 m/s and spatial resolution of 0.1-0.2 mm by Fineberg et al. (1991, 1992). Higher

order accuracy in measuring the crack tip position at very close but discrete time steps revealed the oscillatory nature of the previously presumed constant velocity of the crack tip. However, the crack tip velocity was more or less constant in an average sense. Specimens tested by Fineberg et al. also underwent the mirror to mist to hackle transformation and the formation of roughness on the surface. The high spatial and temporal resolution also helped in showing the strong correlation between velocity oscillations and surface roughness profile.

Surface roughness was also studied by Ravi-Chandar and Yang (1997) on PMMA, Solithane 113 and Polycarbonate. They observed periodic surface band irrespective of the material tested. The formation of these markings, as with branching, is attributed to microcracks. With crack propagation, the length and depth of these markings increased along the crack path.

Crazing at the crack tip is reasoned by Doyle (1983) to be the cause of surface roughness instead of the field of microcracks argument presented by the above researchers. Doyle proposed that the crack propagation was a discontinuous repetition of crack formation and rupture at the crack tip. These rupture of crazes results in release of previously absorbed energy initiating band formation.

In addition to experiments of the crack speed and surface characteristics, experiments have also have been performed on the heat generated by the moving crack tip and the temperature in the process region. Döll (1973) investigated the heat generated in the process zone for fast crack propagation in PMMA. The experiments showed that with the increase in crack velocity the heat generated increased too. Also, the heat generated was also increased with increase in molecular weight of PMMA tested. Measurement of heat generated for lower crack speeds ($0.1c_R$-$0.4c_R$) was performed by Zimmermann et al. (1984). From the experiments they concluded that heat dissipation was the predominant form of dissipation in the process region.

Temperature in PMMA was measured at locations close to the crack path at 10μs, 20μs and 35μs after the crack tip passed certain locations by Fuller, Fox and Field (1975). They measured an average temperature of 455K (after 10μs) in the process zone.

By extrapolation, they calculated the temperature at the running crack tip to be 510K, which is higher than the glass transition temperature of PMMA. This high temperature is enough to induce changes in material properties for example material decomposition leading to formation of gas filled voids very close to the crack tip.

Researchers conducted numerous other experiments - varying the loading rate or using different techniques of crack speed determination or by just experimenting on different materials - to study the dynamic effects of fracture in brittle materials. Early experiments in this field were performed on inorganic glasses but most recent experiments have been on organic polymers. Different experimental techniques for measuring the crack speed e.g. Wallner lines, optical, electric resistance measurements etc., have also been used in this field. Various experimental, analytic and computational aspects of high speed dynamic brittle fracture have extensively been reviewed by Ravi-Chandar (1998) and Fineberg and Marder (1999).

### 1.2.2. Analytic Work Review

Mode – III fracture considerably simplifies the elasticity equations. The out of plane displacement $u_z(x, y)$ is the only non-zero displacement and the only non-zero stress components are $\sigma_{xz}$ and $\sigma_{yz}$. The out of plane displacement $u_z(x, y)$ satisfies the two dimensional distortional wave equation. Analysis of this mode provides considerable insight into fracture process. Hence, many analytic and semi-analytic solutions of Mode-III fracture are available and a few are reviewed below.

The distortional wave equation along with the initial-boundary value problem with rate-independent cohesive constitute law and the crack tip energy balance equations were solved by central difference scheme to study the evolution and effects of process zone on dynamic brittle fracture by Yang and Ravi-Chandar (1996). They showed that the initial development of process zone to be non-steady and the changes in the process zone affects the crack growth processes.

Costanzo and Walton (1997) defined the dynamic Mode-III crack propagation problem as an initial boundary value problem (IBVP). They reduced the dimensionality

of the problem by reformulating the IBVP as a system of integro-differential equations. The integro-differential equations were then solved for elastic and a viscoelastic cohesive zone at the crack tip. Their results show that the rate-independent model failed to capture most of the observed experimental phenomena. However, the rate dependent model presented some interesting feature of experimental observations, but the limiting speed is smaller than experimentally observed value.

The above observations were reaffirmed by solving the integro-differential equations for Mode-III fracture with various rate-independent and rate-dependent cohesive constitutive laws by Costanzo and Walton (1998). They concluded that rate-independent cohesive models do not intrinsically limit the overall crack tip velocity due to the absence of crack tip energy dissipation mechanism. Also, the rate-dependent models do not guarantee that crack will not accelerate to Rayleigh wave speed either. However, the rate-dependent models do retard the acceleration giving a quasi steady state appearance to the crack growth problem.

The research presented in the above two articles was extended to include thermally conducting bodies. Nonlinear temperature dependent cohesive constitutive law at the Mode-III crack tip moving in an unbounded homogeneous linear thermo-elastic medium was numerically investigated by Costanzo and Walton (2002). The results show strong dependence and appearance of forbidden crack velocity range, also predicted by some lattice dynamic models. However, experimentally no forbidden velocity range was observed in dynamic brittle fracture. The response of the crack with temperature dependent cohesive properties was significantly different than that with a purely mechanical cohesive law.

Semi-analytical study of Mode-III fracture was also preformed using three different approaches to solve the integro-differential equations along the fracture plane by Kubair et al. (2003). Results showed crack speeds much lower than theoretical prediction due to the effort of dissipative mechanism in the cohesive zone. In their modeling they also attained increase in stress intensity with increase in crack speed.

Wavy crack model was proposed by Gao (1993) to explain the discrepancy in the observed crack speed and the theoretical predictions. In this model, the crack propagates locally at Rayleigh wave speed along a wavy path, and hence a local high inertia zone, but the macroscopic speed observed is much less than the Rayleigh wave speed, a global low inertia region. Fracture processes observed in experiments such as branching and surface roughness are due to the competition between high inertia zone that develops at the crack tip and the surrounding low inertia zone.

Later, Gao (1996) also proposed a model for dynamic crack propagation in which the near crack tip region wave properties were dependent on the local material tangent modulus and not the macroscopic material properties. Nonlinear continuum mechanics resulted in local Rayleigh wave speed to be lower than the global wave speed, hence, again dividing the continuum to a near crack tip high inertia zone and a surrounding low inertial zone. The analysis showed crack speeds much less than theoretical speeds. Though the model was on the conservative side, it showed the importance of modeling the high inertia zone to understand the fracture processes.

### 1.2.3. Review of Numerical Methods

Johnson (1992) by means of finite element analysis was able to simulate low crack speed and branching observed in high speed brittle fracture. In his simulation, Johnson used dilatation based material damage criterion to define crack propagation and process zone size. In this damage criterion the stiffness of a finite element cell is equated to zero upon reaching a critical volume and thus disregarded or said to have vanished. Crack speeds in the range of experimental observation were achieved. He was also able to simulate micro-branches which preceded successful branching. However, no cohesive zone model was implemented in this simulation.

Finite element discretization based on linear triangular elements arranged in a crossed-triangle quadrilateral pattern with cohesive elements introduced at each element interface was performed on PMMA by Xu and Needleman (1994) under various boundary conditions, mesh refinement and different allowable branch angles. Crack

speeds attained were higher than Rayleigh speed, which is attributed to cohesive surface model and lifting-off mode of separation. In the present work, finite element discretization is based on the work by Xu and Needleman.

Various other computational finite element models involving nodal release technique, moving element procedures, mixed Eulerian-Lagrangian procedure, remeshing procedure and few finite difference and finite volume procedures have been critically reviewed by Nishioka (1997).

### 1.3. Objective

The objective of present research is to model the high inertia zone and simulate observed crack speed and branching phenomenon observed in PMMA under dynamic loading conditions through the development of in-house FEA code.

# 2. FINITE ELEMENT MODELING

In order to simulate the crack speed and branching in brittle materials an in house finite element code was developed using the two-dimensional finite element program discussed by Reddy (2004, 2006). First, an explicit small deformation finite element code with no crack propagation properties was developed and tested with ABAQUS commercial code. Then, a traditional cohesive zone model was implemented and tested. Finally, the small deformation code was upgraded to a large deformation analysis. Thus, again large deformation analysis was test first with no cohesive model and then the already tested cohesive subroutine was integrated. The crack properties with a traditional cohesive model are presented in Section 2.5.

## 2.1. Explicit Formulation

Finite element formulation of the present problem results to solving the hyperbolic equation

$$M\ddot{u} + Ku = F^{ext} \tag{2.1}$$

where $M$ is the mass matrix, $K$ is the stiffness matrix, $F^{ext}$ is the external force vector and $u$ is the displacement vector. Each dot on a variable denotes a time derivative. Here, Equation (2.1) is solved using central difference time integration scheme given by the following equations

$$u_{n+1} = u_n + \Delta t\dot{u}_n + \frac{1}{2}\Delta t^2\ddot{u}_n \tag{2.2}$$

$$\ddot{u}_{n+1} = M^{-1}(F^{ext}_{n+1} - F^{\text{int}}_{n+1}) \tag{2.3}$$

$$\dot{u}_{n+1} = \dot{u}_n + \frac{\Delta t}{2}(\ddot{u}_{n+1} + \ddot{u}_n) \tag{2.4}$$

where

$$F^{\text{int}} = Ku \tag{2.5}$$

and n represents the time step, $\Delta t$ the time increment.

Unlike the implicit schemes, the central difference scheme is conditionally stable. Hence, care should be taken in the selection of time step $\Delta t$ in finite element simulations. The upper limit for the time step, $\Delta t_{cr}$, is given by

$$\Delta t_{cr} \leq \frac{l_e}{c_d} \tag{2.6}$$

where $l_e$ is the shortest distance between two nodes in the mesh as shown in Figure 2.1. And $C_d$ is the dilatational wave speed in the material expressed in terms elastic stiffness $E$, Poisson's ratio $\nu$ and density $\rho$ as (Graff, 1975)

$$c_d = \sqrt{\frac{E(1-\nu)}{\rho(1+\nu)(1-2\nu)}} \tag{2.7}$$

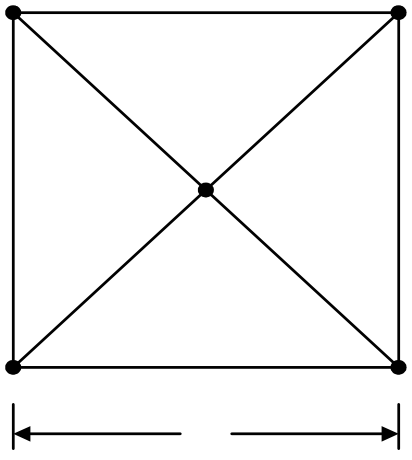

Figure 2.1. Shortest distance between two nodes.

As the time step for explicit scheme is much smaller than that of implicit time integration technique, diagonal mass matrix or lumped mass matrix is used in the former to reduce time in inverting the mass matrix in Equation 2.3. Row-sum lumping is employed in which the elements of each row of a consistent mass matrix are summed and used as the element of the lumped mass matrix.

Keeping in view the main objective of simulation and dynamic fracture including branching, the domain is discretized into square quadrilaterals and each quad is divided into four triangles shown in Figure 2.1. At a later stage cohesive elements are introduced between each element interface in a given mesh, allowing crack propagation through arbitrary directions. Thus, triangular elements have the advantage over quadrilateral elements as the triangular elements allow the crack to propagate through the diagonal of the quad. Hence, any profile of crack branching can be obtained by refining the mesh. In the present work, only three node linear triangular elements are used in all the examples.

## 2.2. Small Deformation Problem

To benchmark the dynamic explicit code with central difference time integration scheme under small deformation, standard problem of a cantilever beam with end load and a simply supported beam under impact load were tested.

### 2.2.1. Deflection Analysis

The traditional problem of a cantilever beam with end load (Figure 2.2) is studied for deflection and compared with ABAQUS. The beam is of length L = 2mm, height H = 0.1mm (Zhang, 2003) and thickness of 0.1mm is subjected to two cases of loading at the free end – constant pulse load (Figure 2.3) and a sine pulse (Figure 2.4) – both for a duration of T, the time period of fundamental vibration for the cantilever beam under plane stress condition (Zhang, 2003). The mesh discretization (80 elements, 62 nodes) is also as shown in Figure 2.2.

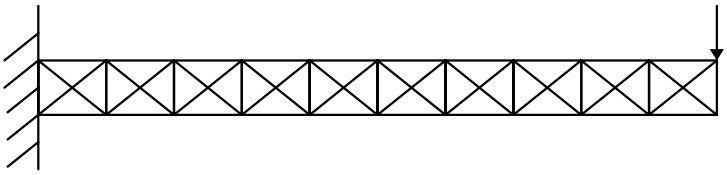

Figure 2.2. Cantilever beam with end load.

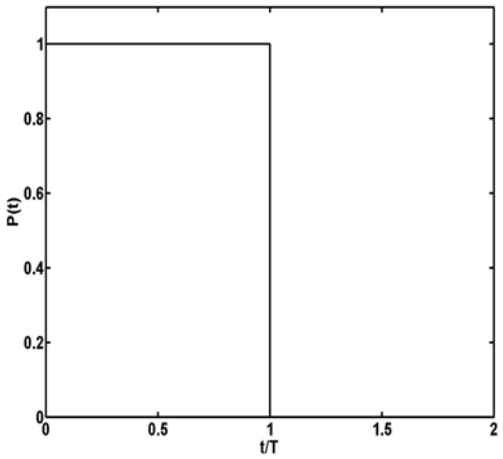


Figure 2.3. Normalized constant pulse load history.

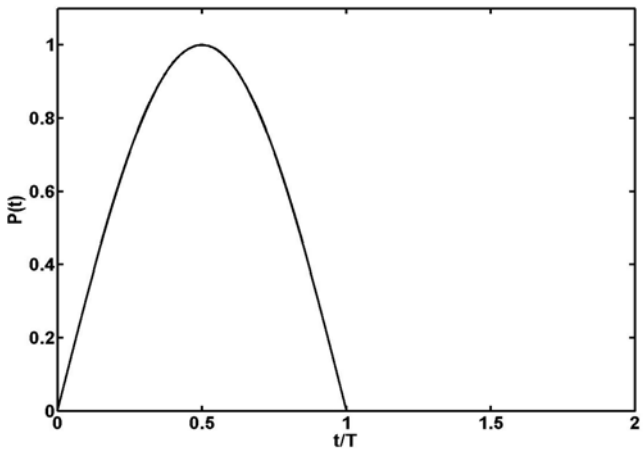


Figure 2.4. Normalized sine pulse load history.

The time period T is a function of material properties $E$ and $\rho$ and geometric properties $A$ the area of cross section, $I$ the moment of inertia and $L$ the length of the beam by Equations (2.8), (2.9) and (2.10).

$$T = \frac{2\pi}{\omega_1} \tag{2.8}$$

$$\omega_1 = \lambda_1^4 \frac{EI}{\rho A} \tag{2.9}$$

$$\lambda_1 = \frac{1.875}{L} \tag{2.10}$$

The displacement results at the point of application of force for the mesh in Figure 2.2 from the present code (efem3t.f – explicit finite element method with three node triangular elements) and for the same mesh from ABAQUS are compared. The time step in both the in-house code and ABAQUS are the same. The time step was forced in ABAQUS to user input by the 'Direct User Control' option under the '*Dynamic' command. The compared displacements from both the codes are presented in Figure 2.5 for the constant load case and Figure 2.6 for the sine pulse load case. The material properties used in the present simulation are tabulated in Table 2.1. As is evident the tip displacements of the in-house code match very well with ABAQUS, for the mesh and time period chosen.

Table 2.1. Material properties used for cantilever problem.

| E (GPa) | $\nu$ | $\rho$ (kg/m$^3$) |
|---|---|---|
| 3.0 | 0.3 | 1000.0 |

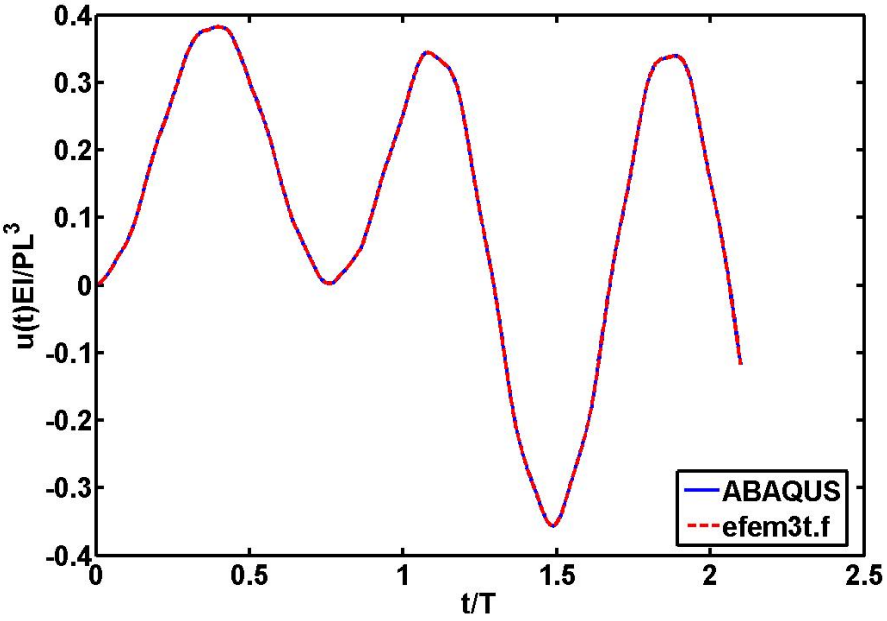


Figure 2.5. Normalized tip deflection under constant pulse load curve.

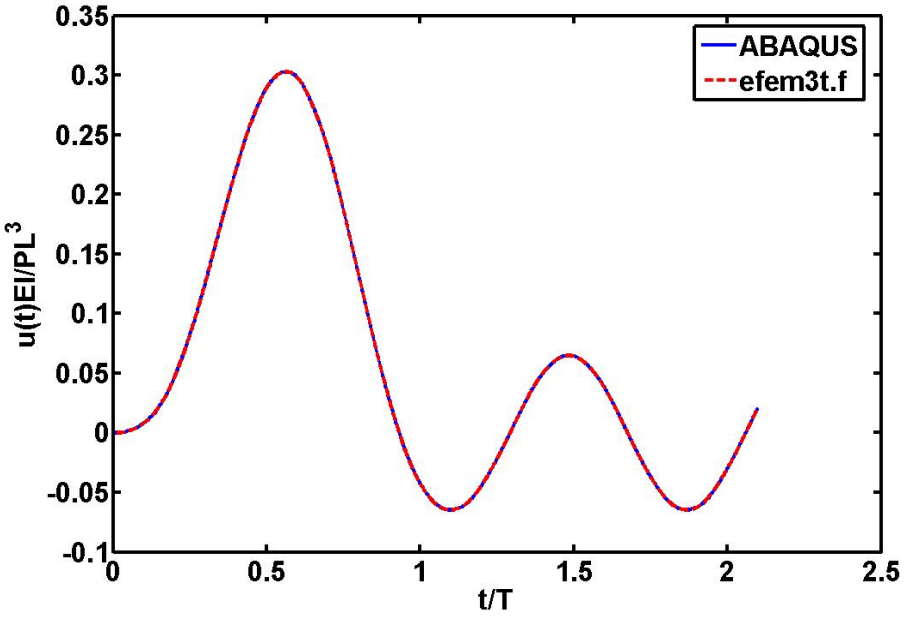


Figure 2.6. Normalized tip deflection under sine pulse load curve.

### 2.2.2. Stress Analysis

With the deflecting and time integration scheme verified, the stress subroutine was tested. Verification of the code was performed by simulating impact loading on a 3-point-bend specimen with length L = 152mm, width W = 37mm, velocity of impact V = 5m/s (Zhang, 2003) and thickness of 1mm as shown in Figure 2.7.

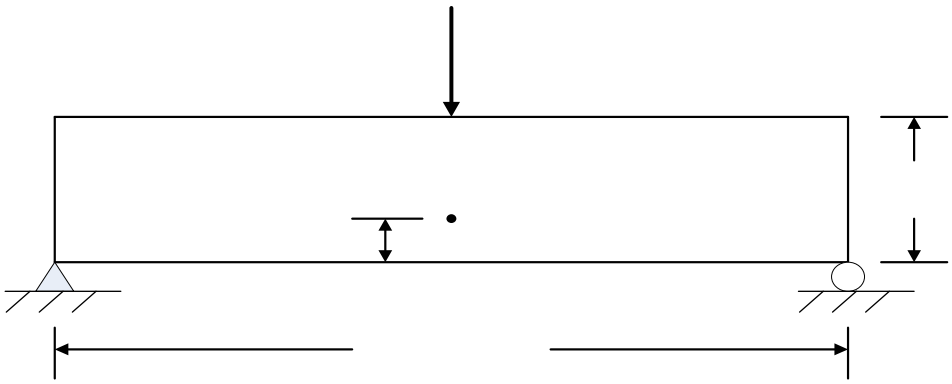

Figure 2.7. Simply supported beam under impact load.

As in the previous case the stress output is compared with ABAQUS. Only half symmetry mesh was simulated. All the inputs including time step in both the programs were given the same values. In addition, the stress output was also compared with results of Zhang (2003). Thus, as in the work by Zhang, stresses are recorded at the gauss point nearest to the center at 0.2W above the base. The material properties are used are tabulated in Table 2.2.

Table 2.2. Material properties used for 3-point-bend problem.

| E (GPa) | $\nu$ | $\rho$ (kg/m$^3$) |
|---|---|---|
| 7.8 | 0.33 | 1500.0 |

The $\sigma_x$ and $\sigma_y$ plots in Figure 2.8 and Figure 2.9 respectively show excellent match with that from ABAQUS under similar conditions and same point of observation. Also, as seen in the $\sigma_x$ plot the point of observation under initially experiences compressive stress at the instance of the arrival of compressive stress wave at normalized time of 0.8. However, after the initial effect, the bending stress has more dominating effect and the stress increases with time. Both the effects were also observed by Zhang. The effects of continuous wave reflections result in development of local crests and troughs as seen in the figure.

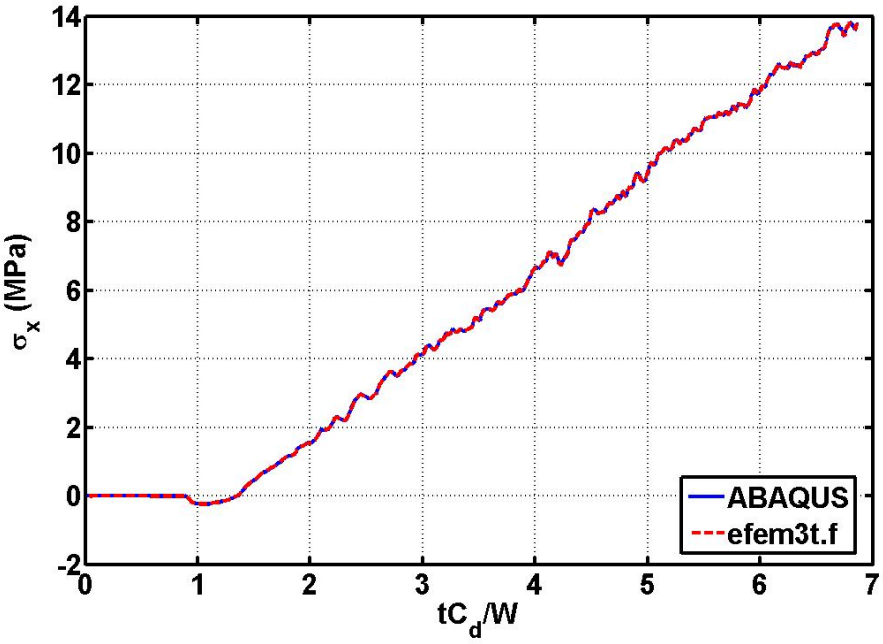


Figure 2.8. Stress $\sigma_x$ plot for a beam under impact load.

The stress response of the specimen in the 'y' direction i.e, $\sigma_y$ (Figure 2.9) is more complex. At normalized time of 0.8, there is a steep drop in the stress due to the arrival of the compressive stress wave. However, with the arrival of the reflected tensile

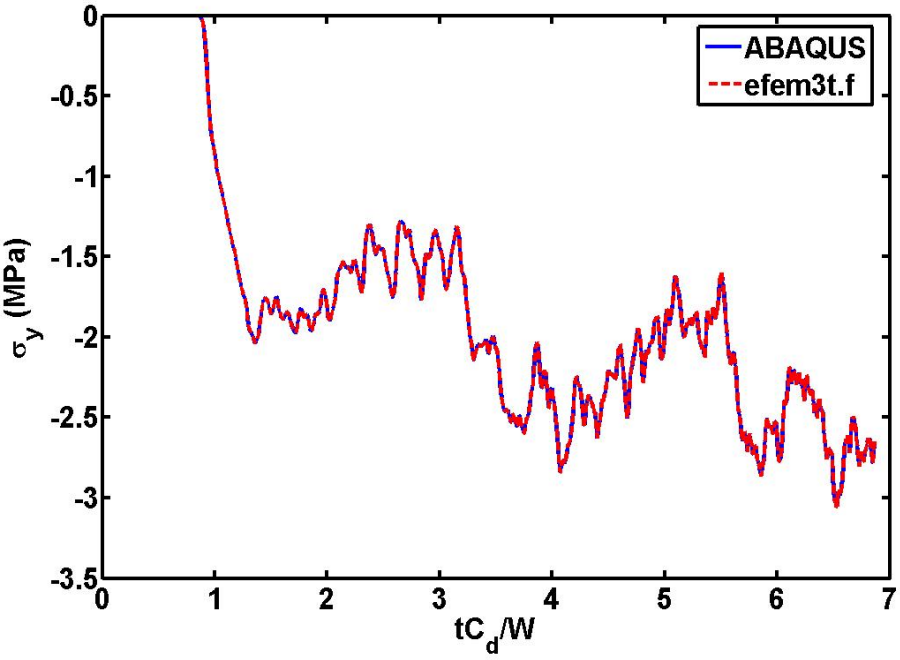


Figure 2.9. Stress $\sigma_y$ plot for a beam under impact load.

wave soon after, there is a slight decrease in compressive stress also observed by Zhang. Thereafter the strong influence of wave interaction is observed. After the slight decrease in compressive stress, the $\sigma_y$ results from the present code and hence ABAQUS, deviate from that of Zhang. This is due to the difference in thickness used, use of linear triangular elements here and quadratic triangle by Zhang, and difference in mesh employed.

### 2.3. Large Deformation Problem

The efem3t.f was updated to eldfem3t.f for dynamic large deformation analysis using Updated Lagrangian formulation with explicit central difference time integration scheme and three node linear triangular elements as discussed in Reddy (2004). Strain energy $U$, kinetic energy $KE$ and external work done $E_{ext}$ are also implemented and computed. The energies are computed as following (Zhang, 2003)

$$U = \frac{1}{2}\int_{\Omega} \sigma_{ij}\varepsilon_{ij} d\Omega \tag{2.11}$$

$$KE = \frac{1}{2} m_i v_i^2 \tag{2.12}$$

$$E_{ext} = \int_{\Gamma} T_i^{ext} \Delta_i^{res} d\Gamma \qquad \text{for force-control problem} \tag{2.13a}$$

$$= \int_{\Gamma} T_i^{react} \Delta_i^{ext} d\Gamma \qquad \text{for displacement-control problem} \tag{2.13b}$$

where $\sigma_{ij}$ and $\varepsilon_{ij}$ are the stress and strain components and $\Omega$ is the volume domain. $m_i$ is the nodal lumped mass of node 'i' and $v_i$ is the corresponding nodal velocity. $\Gamma$ denotes the boundary where external force or displacement is applied, $T_i^{ext}$ is the external force applied and $\Delta_i^{res}$ corresponding resultant displacement for a force-control problems, whereas $\Delta_i^{ext}$ and $T_i^{react}$ are the applied external displacement and resultant reaction force for displacement-control problems.

The cantilever beam mesh shown is Figure 2.2 is analyzed again with a larger end load, the material of the beam is same as before and the properties are as tabulated in Table 2.1. The comparisons of displacement, strain energy, kinetic and external work with ABAQUS are presented in Figures 2.10, 2.11, 2.12 and 2.13 respectively. Again, very good agreement between both the codes is achieved.

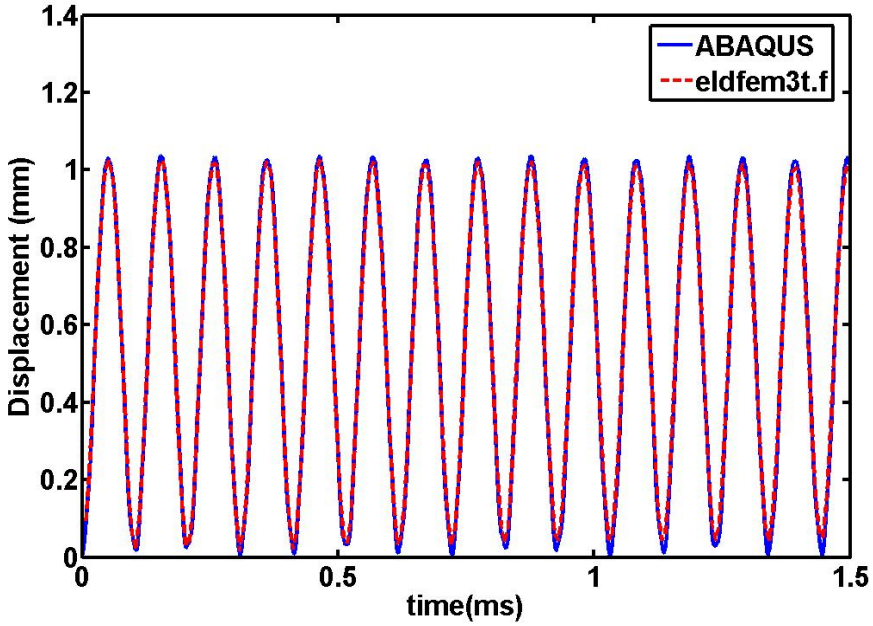


Figure 2.10. Displacement plot for large deformation problem.

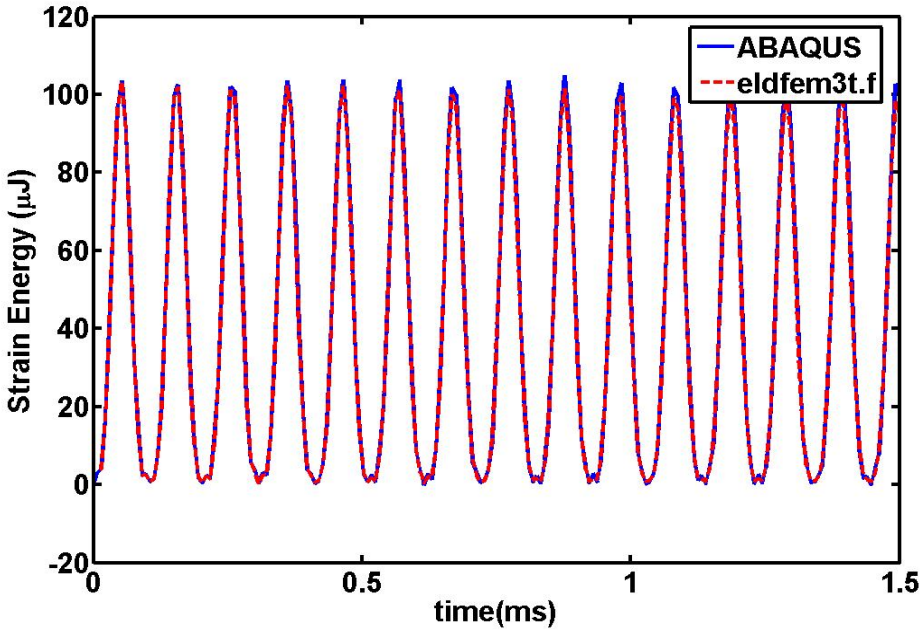


Figure 2.11. Strain energy plot for large deformation problem.

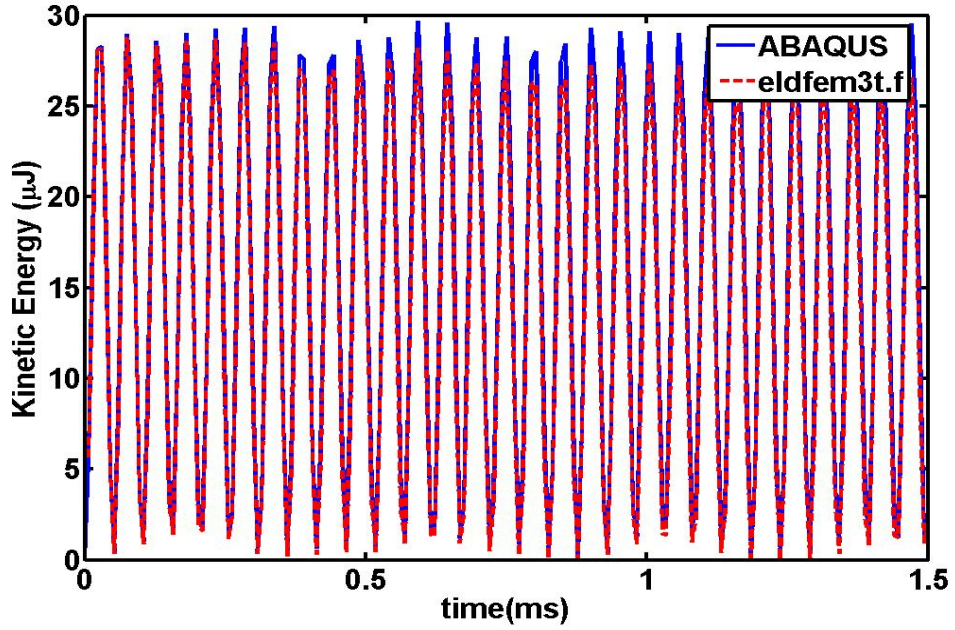


Figure 2.12. Kinetic energy plot for large deformation problem.

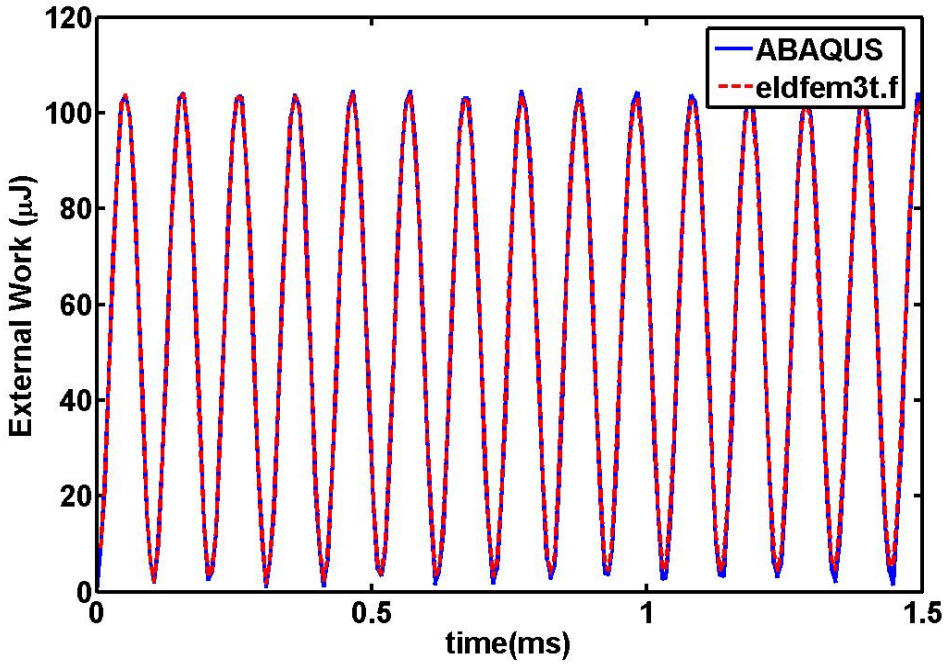


Figure 2.13. External work plot for large deformation problem.

## 2.4. Cohesive Zone Modeling

Cohesive zone model by Roy and Dodds (2001) is implemented in the present work. The energy potential expression or the energy required for interface separation $\phi$ is given by Equation 2.14. And the interface constitutive law is derived from the potential $\phi$. The cohesive constitutive law, given by the Equation 2.15, is a traction-separation relation i.e., the cohesive zone surface traction $t$ is a function of the relative displacement jump across the cohesive surfaces. Diagrammatically, the cohesion constitutive model is presented in Figure 2.14.

$$\phi = e\sigma_c \delta_c \left(1 + \frac{\delta}{\delta_c}\right) e^{-\delta/\delta_c} \tag{2.14}$$

$$t = \frac{\partial \phi}{\partial \delta} = e\sigma_c \frac{\delta}{\delta_c} e^{-\delta/\delta_c} \qquad \text{for loading} \tag{2.15a}$$

$$t = \frac{t_{\max}}{\delta_{\max}} \delta \qquad \text{for unloading} \tag{2.15b}$$

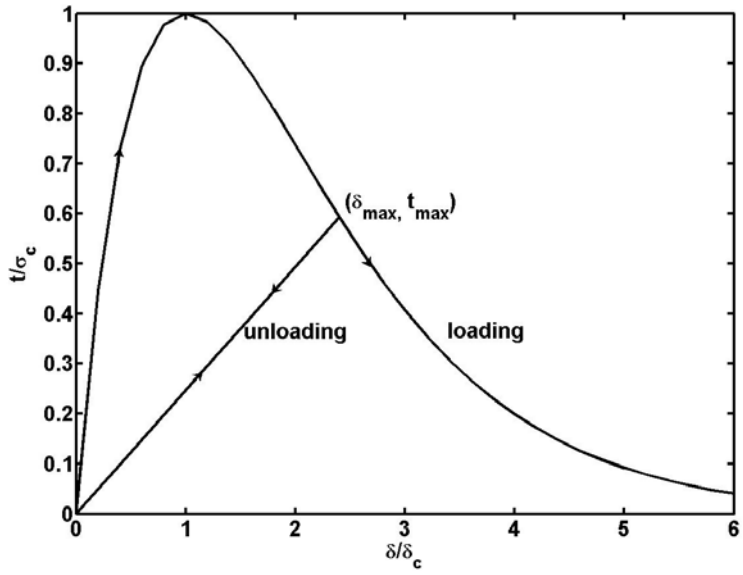


Figure 2.14. Traction separation law (from Roy and Dodds (2001)).

In the above equations $\sigma_c$ is the maximum cohesive traction and $\delta_c$ is the relative displacement at $\sigma_c$. $\delta_{\max}$ and $t_{\max}$ are maximum displacement and traction attained at the instance unloading begins as shown in Figure 2.14. And $\delta$ is the 'effective' opening displacement. $\delta$ is termed 'effective' as it incorporates mixed-mode fracture i.e., $\delta$ is defined in terms of both normal $\delta_n$ and tangential or sliding $\delta_t$ displacement jump across the cohesive surface, given by Equation 2.16.

$$\delta = \sqrt{\delta_n^2 + \beta^2 \delta_t^2} \tag{2.16}$$

The parameter $\beta$ has been introduced by various researchers (Roy and Dodds, 2001; Zhang, 2003 and others) to assign different weights to the sliding and opening displacements. However, under the principle of change of observer, a cohesive zone model with displacement as the only kinematic variable and cohesive traction the only kinetic parameter as in the present model, requires $\beta = 1$ (Costanzo, 1998). Thus, throughout the present work $\beta$ is taken equal to one.

### 2.4.1. Finite Element Formulation

The cohesive element formulation for 3-D problem developed by Roy and Dodds (2001) is adapted to the present 2-D problem. Linear cohesive elements are introduced at every element interface. The local cohesive element node numbering and the local coordinate system are shown in Figure 2.15.

The displacement vector, $\bar{u}$ is presented in Equation 2.17. The superscript 'R' denotes 'Right side of $\xi$-axis' and 'L' denotes 'Left side of $\xi$-axis', the subscript '1' denotes tangential direction and '2' denotes normal and 'T' denotes transpose.

$$\bar{u} = [u_1^R \;\; u_1^L \;\; u_2^R \;\; u_2^L]^T \tag{2.17}$$

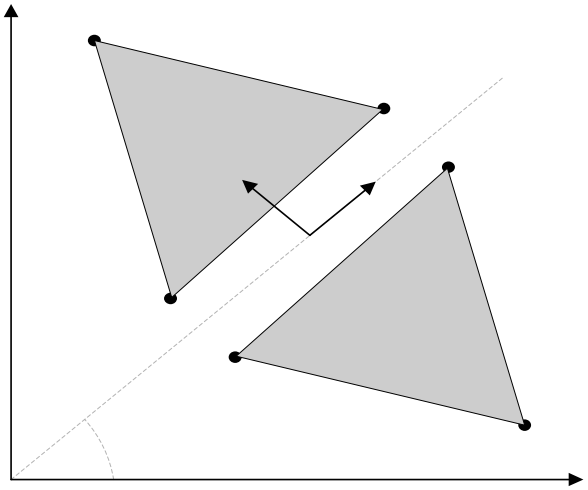

Figure 2.15. Cohesive element representation.

The displacement vector, $\bar{u}$, is further expressed, as in Equation 2.18, in terms of the finite element interpolation matrix $N$ and nodal displacement vector $\bar{d}$ (Roy and Dodds, 2001). In Equation 2.20 the superscript denotes the node numbers as shown in Figure 2.15. However, the subscripts have to same meaning as in Equation 2.16.

$$\bar{u} = \underset{\sim}{N}\,\bar{d} \tag{2.18}$$

where $N$ and $\bar{d}$ are expressed as

$$\underset{\sim}{N} = \begin{bmatrix} N_1 & 0 & 0 & 0 & N_2 & 0 & 0 & 0 \\ 0 & 0 & N_1 & 0 & 0 & 0 & N_2 & 0 \\ 0 & N_1 & 0 & 0 & 0 & N_2 & 0 & 0 \\ 0 & 0 & 0 & N_1 & 0 & 0 & 0 & N_2 \end{bmatrix} \tag{2.19}$$

$$\bar{d} = \begin{bmatrix} u_1^1 & u_2^1 & u_1^3 & u_2^3 & u_1^2 & u_2^2 & u_1^4 & u_2^4 \end{bmatrix}^T \tag{2.20}$$

$N_1$ and $N_2$ in Equation 2.19 are the interpolation functions for linear elements given as

$$N_1 = \frac{1}{2}(1-\xi) \tag{2.21a}$$

$$N_2 = \frac{1}{2}(1+\xi) \tag{2.21b}$$

Thus, the cohesive element is linear in a finite element interpolation sense given by Equation 2.21, but the governing constitutive law (Equation 2.15) is nonlinear.

The relative displacement jump vector $\Delta\bar{u}$, between opposite cohesive surface in the global coordinates is obtained by introducing operator matrix $L$ (Roy and Dodds, 2001). The matrix $L$ for the present 2-D problem is given in Equation 2.23.

$$\Delta\bar{u} = \underset{\sim}{L}\,\underset{\sim}{N}\,\bar{d} \tag{2.22}$$

where

$$\underset{\sim}{L} = \begin{bmatrix} +1 & -1 & 0 & 0 \\ 0 & 0 & +1 & -1 \end{bmatrix} \tag{2.23}$$

Finally, the local separation vector $\bar{v}$, the $\underset{\sim}{B}$ matrix and nodal force vector $\bar{f}$ are as given by Roy and Dodds (2001) without any further changes.

$$\bar{v} = \underset{\sim}{B}\,\bar{d} \tag{2.24}$$

$$\underset{\sim}{B} = \underset{\sim}{R}\,\underset{\sim}{L}\,\underset{\sim}{N} \tag{2.25}$$

$$\bar{f} = \int_{-1}^{1} \underset{\sim}{B}^T\,\bar{t}\,J\,d\xi \tag{2.26}$$

Three Gauss points are used in the evaluating the integral in Equation 2.24. Also, $J$ is the Jacobian of transformation, $\bar{t}$ is the cohesive traction vector - related to the traction-separation law - is give by Equation 2.26 and $\underset{\sim}{R}$, Equation 2.27, is the coordinate transformation matrix.

$$\bar{t} = \begin{bmatrix} t_t \\ t_n \end{bmatrix} = \begin{bmatrix} \frac{t}{\delta}\delta_t \\ \frac{t}{\delta}\delta_n \end{bmatrix} \tag{2.27}$$

$$\underset{\sim}{R} = \begin{bmatrix} \cos\theta & \sin\theta \\ -\sin\theta & \cos\theta \end{bmatrix} \tag{2.28}$$

### 2.4.2. Verification

Two problems were solved on a plate of 0.2 × 0.4mm dimension with eight identical elements (Zhang, 2003) to verify the cohesive zone implementation. PMMA material properties were used which are presented in Table 2.3 (Xu, et al., 1994).

Table 2.3. PMMA material properties.

| E (GPa) | $\nu$ | $\rho$ (kg/m$^3$) | $\sigma_c$ (MPa) | $\delta_c$ (μm) |
|---|---|---|---|---|
| 3.24 | 0.35 | 1190.0 | 324.0 | 0.4 |

Force controlled (Figure 2.16) and a displacement controlled (Figure 2.17) problems are considered. Cohesive zone elements are introduced in a mesh *a priori* at all element interfaces as first introduced by Xu and Needleman (1994). The thicker lines in Figures 2.16 and 2.17 indicate the presence of cohesive elements.

First, a small force F which does not lead to fracture in the plate is applied as shown. Under ideal conditions of force transmission across the cohesive elements the displacements at every node under same boundary, force and material properties, should be equal to the case with same mesh but no cohesive element but all elements bonded in the traditional FEA sense. The displacements at Position-1 and Position-2 (position 2 is to the left of central element interface) are compared with 'with' cohesive zone elements (w cze) and 'without' (or fully bonded) cohesive zone elements (w/o cze) and are presented in Figure 2.18 and Figure 2.19.

Similarly, displacement controlled problem with velocity boundary condition is analyzed. Again, the displacements at Node # 1 and Node # 2 are compared with and without cohesive elements and are presented in Figure 2.20 and Figure 2.21.

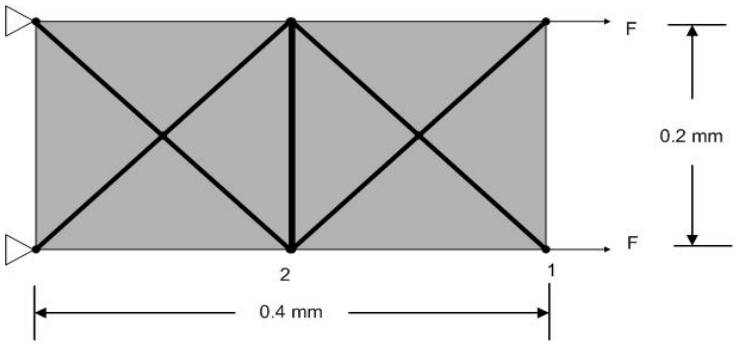


Figure 2.16. Force controlled problem.

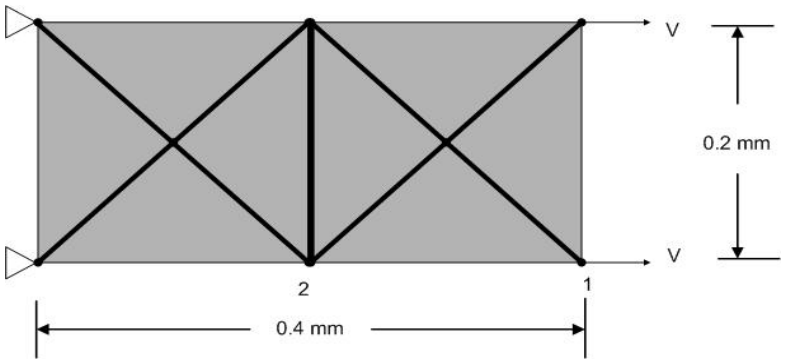


Figure 2.17. Displacement controlled problem.

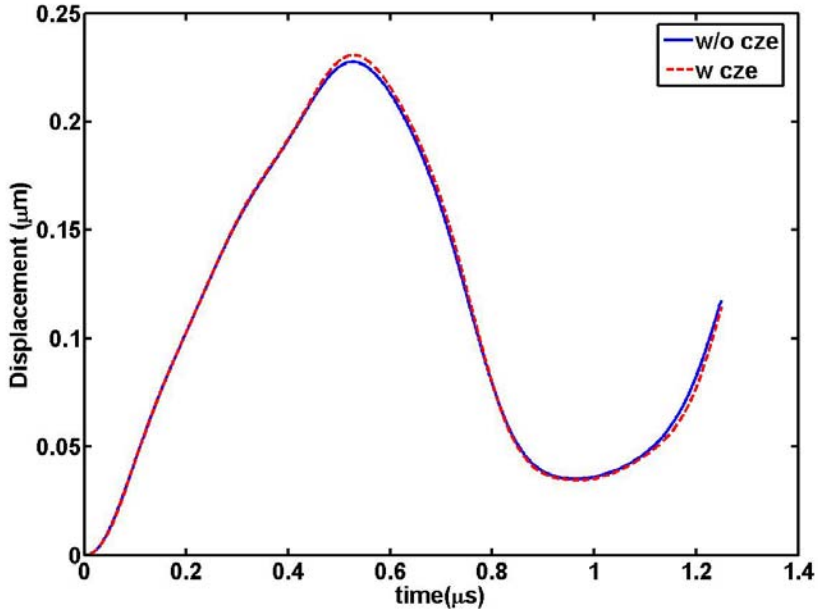


Figure 2.18. Displacement check at Position-1 for force controlled problem.

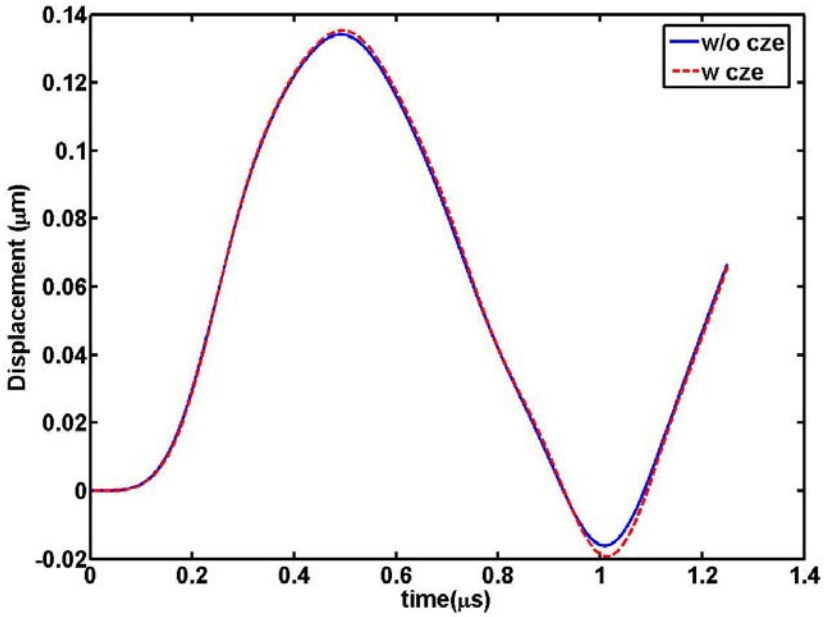


Figure 2.19. Displacement check at Position-2 for force controlled problem.

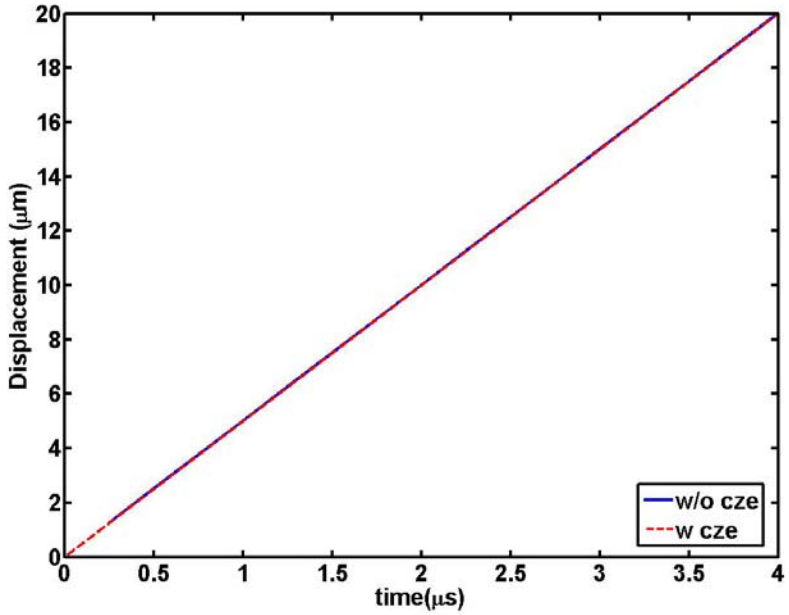


Figure 2.20. Displacement check at Position-1 for displacement controlled problem.

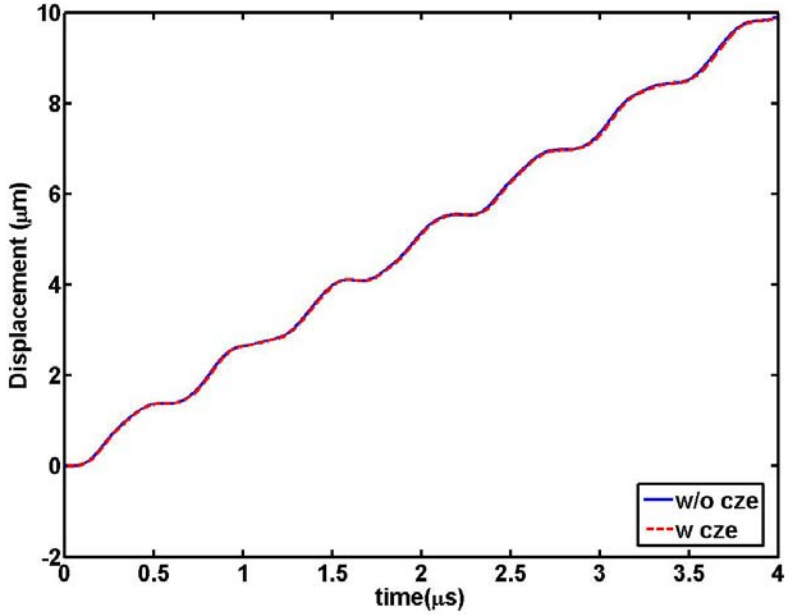


Figure 2.21. Displacement check at Position-2 for displacement controlled problem.

There are slight deviations in the displacements especially prominent in the force controlled problem with displacement measured at Node # 2, Figure 2.19 and to a lesser extant in Figure 2.18. This is due to the energy dissipation with deformation in the cohesive elements. However, the comparison of displacements between with and without cohesive elements mesh shows good match.

## 2.5. Dynamic Brittle Fracture

After the verification of the FEM code and the implementation of the cohesive model, the dynamic brittle fracture problem is studied for crack velocity and branching properties. Large displacement finite element analysis is performed.

### 2.5.1. Problem Description

A rectangular plate of 4 × 1.2 × 1mm dimensions made of PMMA, material properties presented in Table 2.3, with a center crack of 0.4mm length is analyzed under plan strain conditions for symmetric velocity loading on the upper and lower surfaces as shown in Figure 2.22.

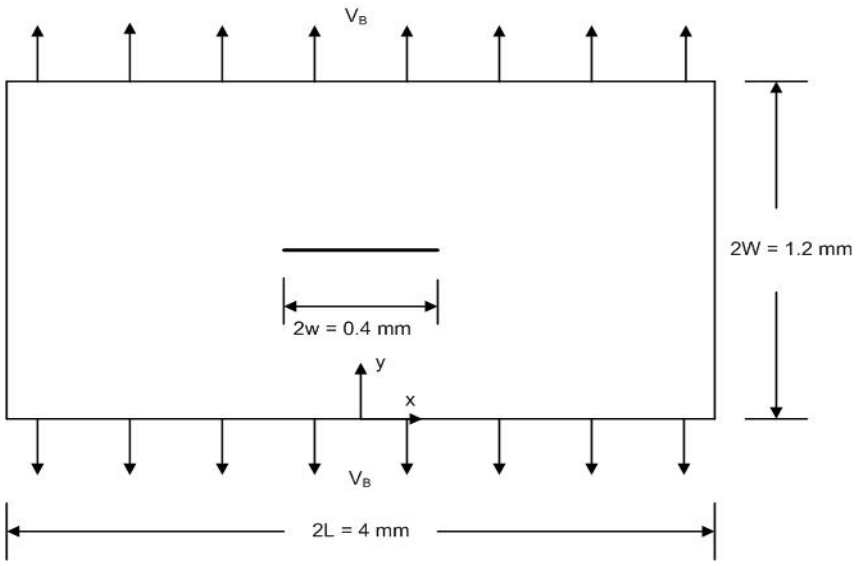


Figure 2.22. Specimen dimensions and boundary condition.

For the above plate, only the right half of domain is discretized, keeping in view the geometric and load symmetry about the y-axis. The right half is discretized into square quadrilaterals of edge length 20μm and each quad is divided into four linear triangular displacement elements as shown in Figure 2.23. Cohesive elements are introduced at each element interface which lies within a rectangular region to the right of the crack tip as shown by thicker lines.

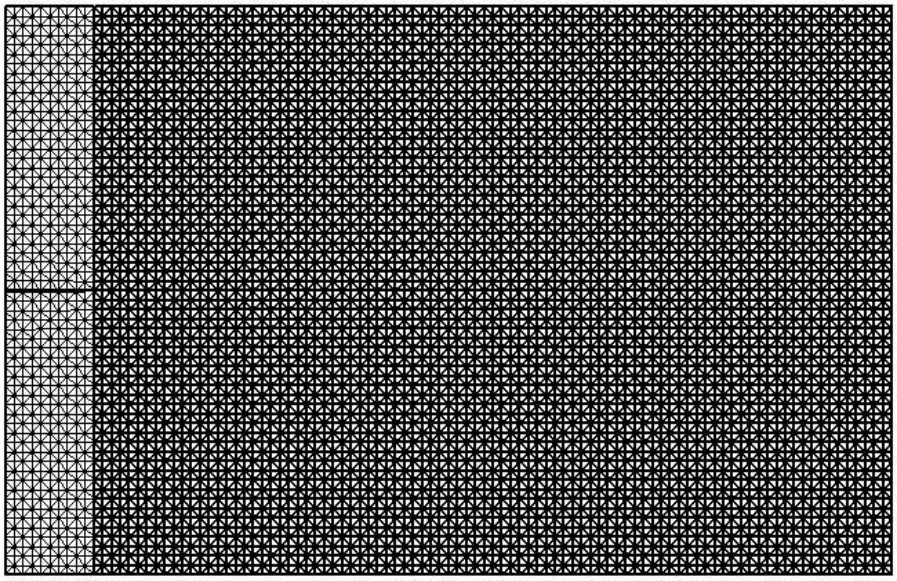

Figure 2.23. Mesh used for dynamic fracture problem.

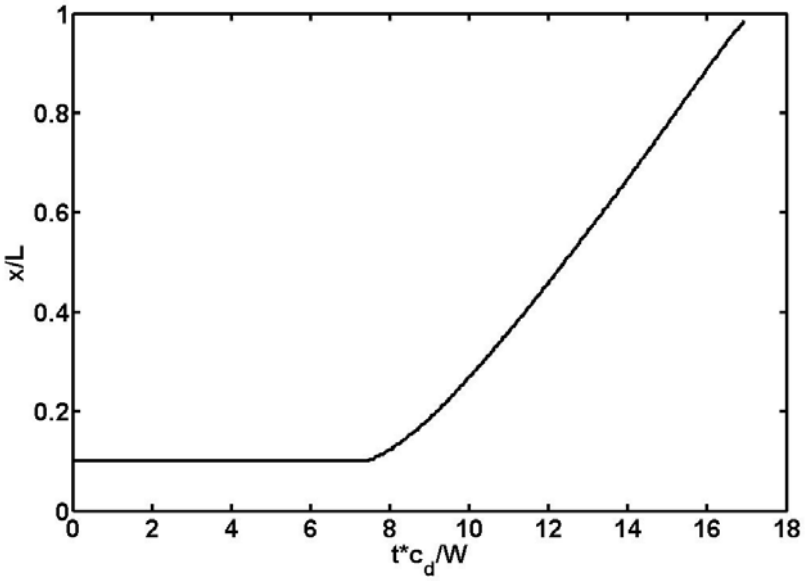


Figure 2.24. Normalized crack tip position versus time for $V_B$ = 5 m/s.

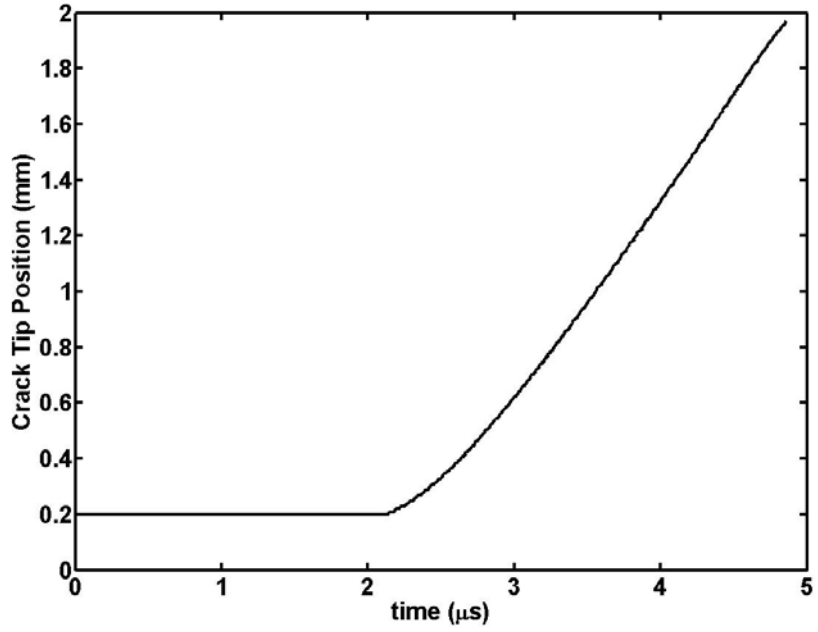


Figure 2.25. Crack tip position versus time for $V_B$ = 5 m/s.

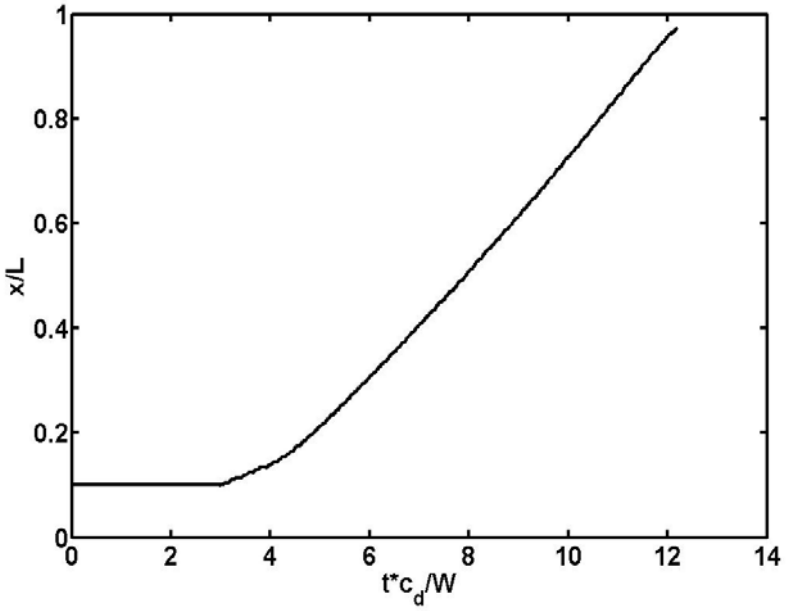


Figure 2.26. Normalized crack tip position versus time for $V_B$ = 10 m/s.

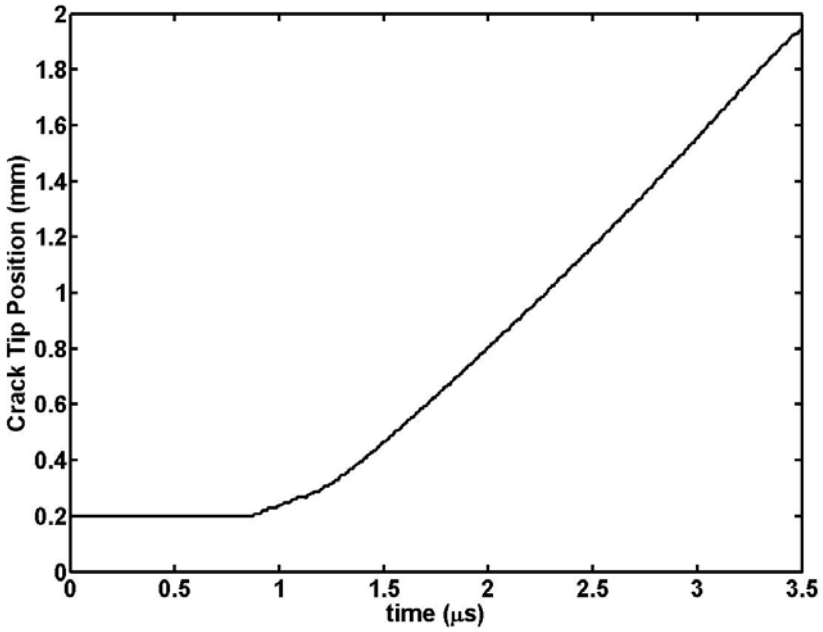


Figure 2.27. Crack tip position versus time for $V_B$ = 10 m/s.

Stability of the numerical simulation is governed by the Equation 2.6. With the introduction of cohesive elements the stability becomes more critical and results in the further reduction of $\Delta t_{cr}$. Thus, in the present simulation the time step used was of the order of $\Delta t_{cr}/10$.

Two velocity boundary conditions were studied: 5m/s and 10m/s. The crack tip position plots for the two cases are presented in Figure 2.24/Figure 2.25 and Figure 2.26/Figure 2.27, respectively. No branching was observed. The crack speed calculated from the above profiles was 694m/s (= $0.74c_R$) for $V_B$ = 5m/s case and 720m/s (= $0.77c_R$) for $V_B$ = 10m/s case. The Rayleigh wave speed was calculated for PMMA from Equation 2.28 (Graff, 1975).

$$c_R = \frac{0.87 + 1.12\nu}{1+\nu} c_s \tag{2.29}$$

where $c_s$ is the shear wave speed given by

$$c_s = \sqrt{\frac{\mu}{\rho}} \tag{2.30}$$

# 3. MODELING OF HIGH INERTIA ZONE

Many of the mechanisms for branching, surface roughness, low crack speed in dynamic brittle fracture have not been completely explained. These observed phenomena are credited to the nucleation, growth and coalescence of microcracks. The formation of microcracks is a result of intense crack tip stress intensity, which induces nucleation of flaw in the structure. These flaws coalesce to form microcracks and microbranches (Ravi-Chandar et al., 1984b; Ravi-Chandar 1998). Though these microcracks play an important role in the fracture process, the present work is of view that the modeling of material evolution very near to the crack tip is also a key component to the understanding of dynamic brittle fracture.

## 3.1. High Inertia Zone: Definition and Modeling

In experiments on specimens softened with holes (flaws) (Washabaugh and Knauss, 1994) the crack propagation attained near Rayleigh wave speed with high unsteady behavior as the presence of holes close to the crack propagation path resulted in redistribution of damage away from the crack tip. Thus, in the absence of excessive damage at the crack tip, continuum analysis is valid in brittle fracture. Same conclusion can be drawn from the semi-analytic work on Mode-III fracture by Costanzo and Walton (1997, 1998, 2002) and Kubair et al. (2003). These researchers showed that through appropriate choice of rate-dependent cohesive model, which represents cohesive zone material (atomic) constitutive law, crack speed less than Rayleigh wave speed can be attained.

Johnson (1992) by performing finite element analysis of near tip region using volumetric criterion for damage, was successful in simulating low crack speed and branching. Though Johnson attributed the individual cell damage to nucleation of microcracks, there was no specific nucleation model implemented in the analysis. The reduction of stiffness in this analysis can also be ascribed to continuous accumulation of damage at the crack tip.

Measurement of temperatures higher than the glass transition temperature (Fuller et al., 1975) very close to the crack tip is an indication to rearrangement of local material structure from that of the global. The stress near crack tip region in a dynamically moving crack can be characterized by inertia parameter $v/c_s$, where v is the crack speed and $c_s$ shear wave speed given by the Equation 2.29. Gao (1996), proposed a model in which the crack response is governed by the local inertial/material properties. Structural changes at the crack tip result in local wave speeds that are lower than the surrounding global (or apparent) properties. The crack response is governed by material tangent modulus at the near-tip high inertia zone (term first introduced by Gao, 1993) and not on microcrack interaction. Thus, the local "c" shear modulus $\mu_c < \mu_a$ , the apparent "a" shear modulus and hence the local wave velocity being the less than the global velocity, i.e., $(c_s)_c < (c_s)_a$. The inertia parameter $(v/c_s)_c > Y$ forming a high inertia zone around the crack tip and $(v/c_s)_a < Y$ a global low inertia zone. Where Y = 0.6-0.7 is the ratio of $v/c_s$, exceeding which the hoop stress $\sigma_{\theta\theta}$ attains a maximum around $\theta = \pm 60^o$. Using nonlinear continuum analysis to model near crack tip high inertia zone, Gao showed that lower limiting speed can be attained.

Thus, experimental, analytic and computational results show that near tip region or the high inertia zone plays an important role towards attaining low crack speeds and continuum analysis is valid provided local material properties are properly modeled.

The region surrounding the crack tip where predominantly all the energy is dissipated is termed as the process region or process zone, size of which is typically in the order of 100μm (Ravi-Chandar, 1998). There are not enough references in literature for the equivalence of high inertia zone and the process zone. However, it is known that the process region grows normal to the direction of propagation (Johnson, 1992) with increasing loads. The high inertia region is assumed to be region ahead of the crack tip hence in the direction of propagation. Here distinction is made between the two; it is assumed that the high inertia region to be very close to the crack tip but smaller than the process zone and hence inside the process zone.

Fracture behavior in brittle material is predicted well by linear elasticity theory for low crack velocities. This shows that the high inertia zone is not active under all circumstances - there is not enough accumulation of damage for a predominant shift from global properties. Tests on Homalite-100 showed that a crack traveling below critical speed increased velocity on interaction of reflected stress waves and remained unaffected by further arrivals of stress waves (Ravi-Chandar and Knauss, 1984c). This suggests that high inertia zone is activated above a critical energy or stress limit and is an irreversible process, thought the interaction with reflected waves is not mandatory.

In the present research high inertia zone at the crack tip is modeled as an additional term is added to the cohesive model proposed by Roy and Dodds (2001). Mathematically, the high inertia region is modeled as monotonically increasing stress intensity cohesive term. This term is taken to be a function of the total energy per unit volume input into the system. Though the crack propagation properties are a function of energy input into the crack tip region, system energy is taken into consideration for computational convenience and is purely phenomenological. Thus, the modified cohesive traction is

$$t = \sigma^{e} + \sigma^{ir} \tag{3.1}$$

where

$$\begin{aligned} \sigma^{e} &= e\sigma_{c}\frac{\delta}{\delta_{c}}e^{-\frac{\delta}{\delta_{c}}} \\ \sigma^{ir} &= T(E)\frac{\delta}{6\delta_{c}} \end{aligned} \tag{3.2}$$

where $E$ is the total work done per unit volume on the system and $T(E)$ is any function relating the total work done to the cohesive traction. The traction $T(E)$ is distributed

linearly along the cohesive zone with a maximum at the crack tip. The definitions of $\sigma^e$ and $\sigma^{ir}$ are borrowed from Costanzo and Allen (1995) and are presented below-

> $\sigma^e$ is assumed to originate from the interface free energy and, in this sense, to be the expression of mechanically reversible transformations, such as bond stretching in crystalline materials or fibril elastic stretching in polymer crazing. $\sigma^{ir}$ is not assumed to have an explicit and one-to-one relationship with the interface opening displacement. This allows the interface to transfer forces of various intensity even under the assumption of perfect cohesion, i.e. a situation characterized by a null opening displacement. The physics behind the irreversible part of the cohesive force $\sigma^{ir}$ depends on the particular system at hand. For example, in the case of single craze formation, $\sigma^{ir}$ can represent the average effect of the forces responsible for the craze nucleation through secondary bond breakage.

In the present work, $\sigma^{ir}$ represents the homogenization of the energy associated with various dissipative processes occurring at the crack tip due to high inertia zone.

### 3.2. Results

Two cases with applied boundary velocities equal to 5 m/s and 10 m/s are performed for the same geometric properties (Figure 2.22), finite element mesh (Figure 2.23) and material properties (Table 2.3) as described in the Section 2.5.

The high inertia cohesive term for the 5m/s boundary case is shown in Figure 3.1 and Figure 3.2 and for the 10 m/s boundary case in Figure 3.3 and Figure 3.4. The shape of $T(E)$ was found by heuristic processes to be piecewise linear with three distinct phases – Phase- I, Phase-II and Phase-III – before the initiation of branching.

As evident from these figures, the high inertia region is modeled as continuously increasing stress intensity term. This region is activated in $V_B$ = 5 m/s at non-dimensional time ($t^*c_d/W$) of 8.53. Phase-I is active till 10.1, Phase-II till 11.8 and Phase-III till 17.24. And the corresponding non-dimensional times for 10 m/s case are 4.52, 6.1, 7.66 and 8.7. For each phase, $T(E)$ is chosen to be a linear curve and are of the form

$$T(E) = mE + c \tag{3.3}$$

where $m$ is the slope and $c$ is any constant.

Due to symmetries about a mode I crack, the rupture of bonds and the critical state of deformation should occur right in front of the crack tip (Gao, 1996). As there is no experimental or analytic measure of the size of high inertia region, in the finite element formulation, this region is approximated to be linear with a length of four cohesive elements. Thus, new cohesive force term, $\sigma^{ir}$, was applied to only to the cohesive element undergoing separation and three cohesive elements in front of the crack tip. But, $\sigma^{e}$ is present at every element to element interface in the fracture region of the mesh as described in Section 2.5. Also, the crack is considered to have propagated if the relative displacement of opposite crack faces is greater than $6\delta_c$ (Roy and Dodds, 2001).

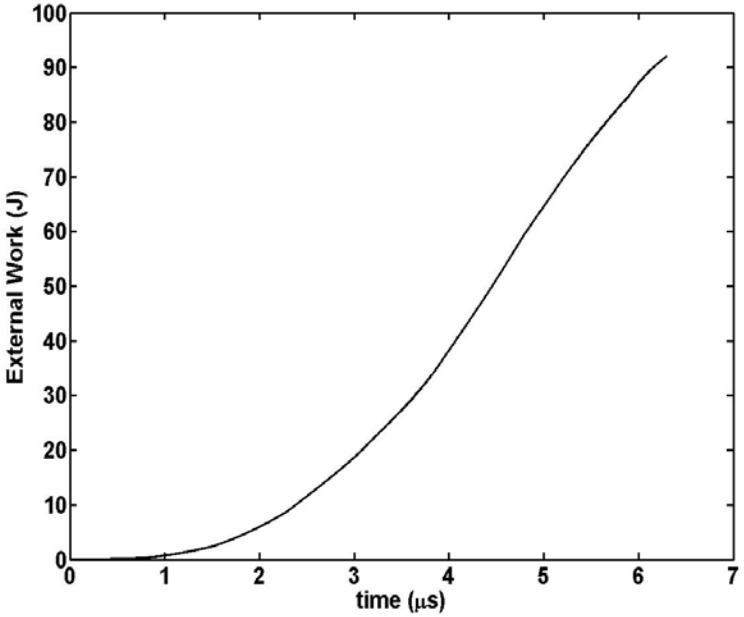


Figure 3.1. Energy-time curve for $V_B$ = 5 m/s.

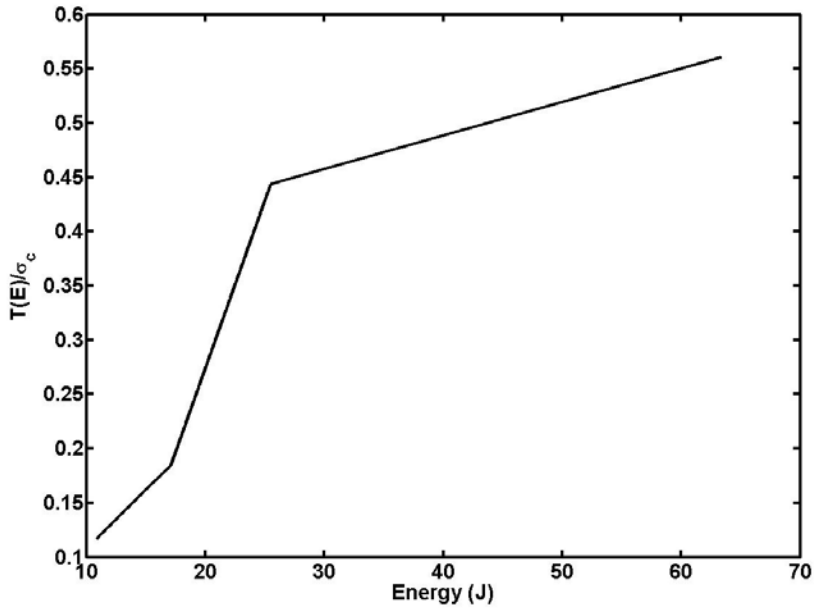


Figure 3.2. High inertia zone cohesive traction for $V_B$ = 5 m/s.

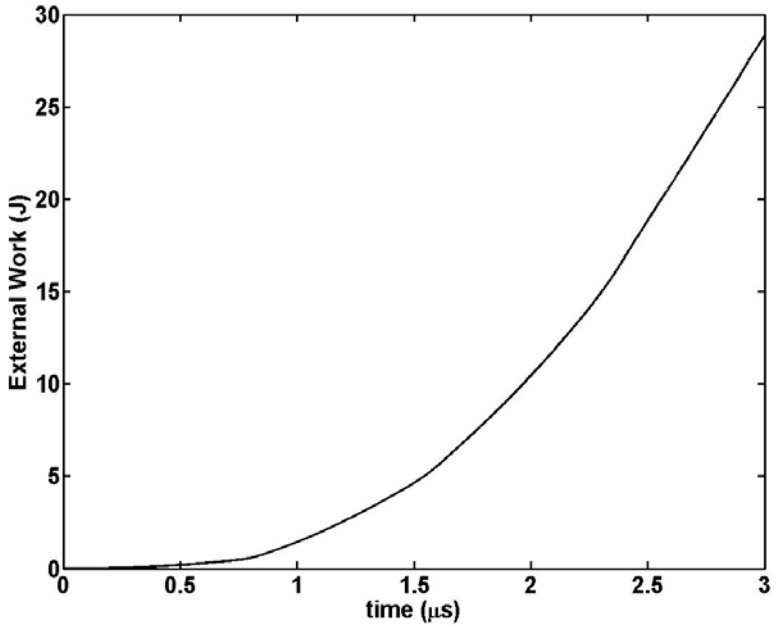


Figure 3.3. Energy-time curve for $V_B$ = 10 m/s.

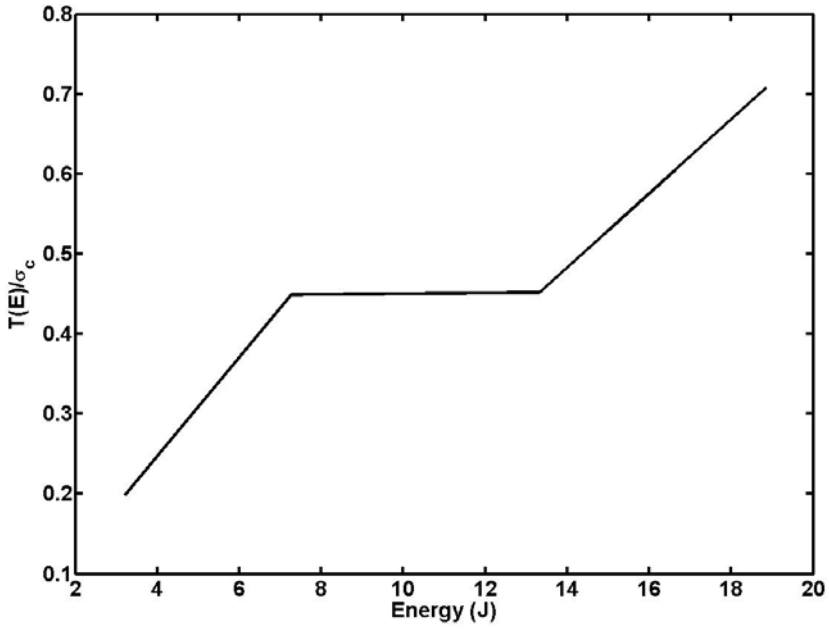


Figure 3.4. Dissipative cohesive traction curve for $V_B$ = 10 m/s.

### 3.2.1. Branching

As evident from the above plots, the stress intensity factor in Phase-III is higher than in Phase-II which is higher than that of Phase-I. Experimentally, Ravi-Chandar and Knauss (1984b), by studying the caustics observed that the stress intensity in hackle zone was higher than the mist which is higher than the mirror zone as predicted above in each of the phases. Also, in this formulation, branching occurred at the end of Phase-III, just as in experiments where branching was observed at the end of hackle pattern (Ravi-Chandar and Knauss, 1984b). Thus, the equivalence of Phase-I, Phase-II and Phase-III to 'mirror', 'mist' and 'hackle' respectively is very striking.

In the present simulation, branching was initiated when the ratio of $T(E)$ and material cohesive strength $\sigma_c$ attained a critical value, dependent on the geometry and boundary conditions. For the $V_B$ = 5 m/s branching was initiated at $T(E)/\sigma_c = 0.55$ and for $V_B$ = 10 m/s at $T(E)/\sigma_c = 0.70$. In the absence of $\sigma^{ir}$, the crack quickly attained near Rayleigh wave speed and no branching was observed - results for this case in which $\sigma^{ir}$ is not accounted for is presented in Section 2.5.

On branching, the crack tends to travel parallel to the initial crack propagation direction along the next element interface. Again, in the absence of $\sigma^{ir}$ at crack tip on this interface, the crack propagates in straight configuration along this layer with no further branching and the speed attains near Rayleigh wave speed. And with application of $\sigma^{ir}$ on the new layer the crack jumps to the next element interface and so on. The final branch profiles for the boundary conditions are presented in Figures 3.5 and 3.6.

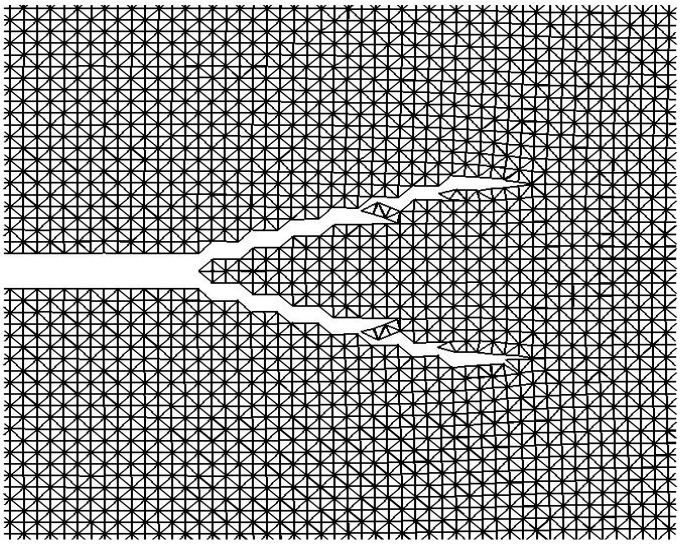

Figure 3.5. Final branch profile for $V_B$ = 5 m/s.

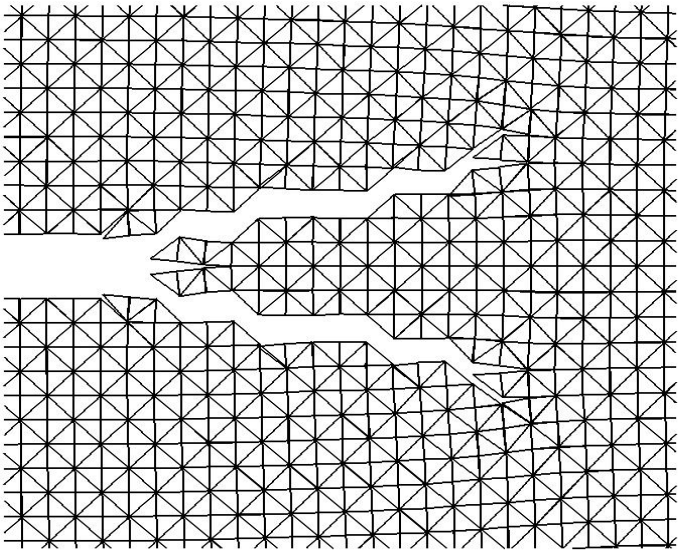

Figure 3.6. Final branch profile for $V_B$ = 10 m/s.

This ‘jump’ to the next element interface level in the branching process is interpreted as the transport of crack tip from one group of parallel microcracks to another. This process is in agreement with observations of high speed photomicrographs that indicate that the branching starts from microcracks that are initially parallel to the main crack front (Ravi-Chandar and Knauss, 1984b). Though the microcracks are not responsible for branch initiation but the distribution of (parallel) microcracks defines the branch profile. Thus, the mechanism of branching proposed here is that of a combined work by high inertia crack tip and microcracks - high inertia zone initiates branching, due to continuous increase in stress intensity factor, and the presence of microcrack defines the angle of branching. It is postulated that with the knowledge of distance between parallel microcracks and the main crack or the branch profile could give a good estimate of the high inertia zone size.

Various failed attempts to branching were also recorded. An example is presented in Figure 3.7 and Figure 3.8. In Figure 3.7 there are two active branches at t = 2.45 μs ($V_B$ = 10 m/s), however, at t = 2.6 μs the left branch is fully arrested and the right branch attempt develops into a successful branch.

Also the branch profile was dependent on the choice of ‘m’. The effect of choice of ‘m’ for third element-element interface above and below the main crack interface is shown in Figure 3.9 and 3.10. In Figure 3.9 a smaller value of ‘m’ for Level 3 was used than that for the same level in Figure 3.10. We see that with the use of a higher ‘m’, the crack tip does not propagate along Level 3 but jumps one level up. Thus, the branch profile is statistical in nature and dependent on the value of ‘m’ chosen.

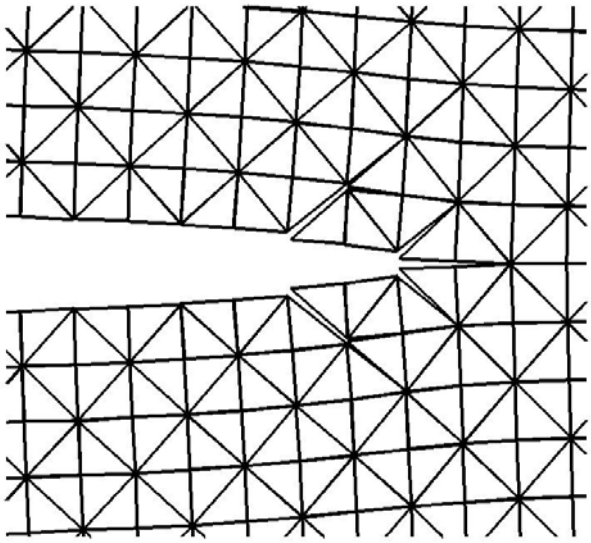

Figure 3.7. Attempted branching t = 2.45μs, $V_B$ = 10 m/s.

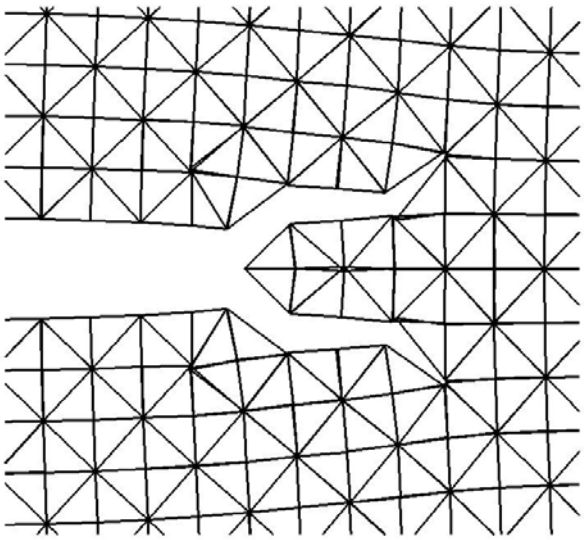

Figure 3.8. Successful branching t = 2.60μs, $V_B$ = 10 m/s.

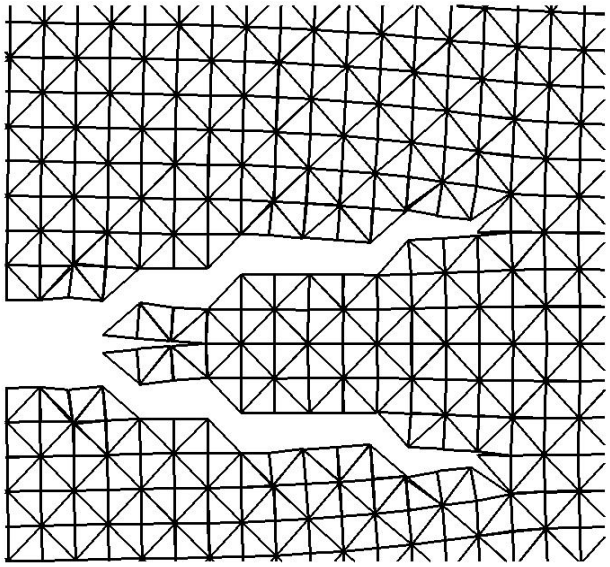

Figure 3.9. Branch opening of level-3.

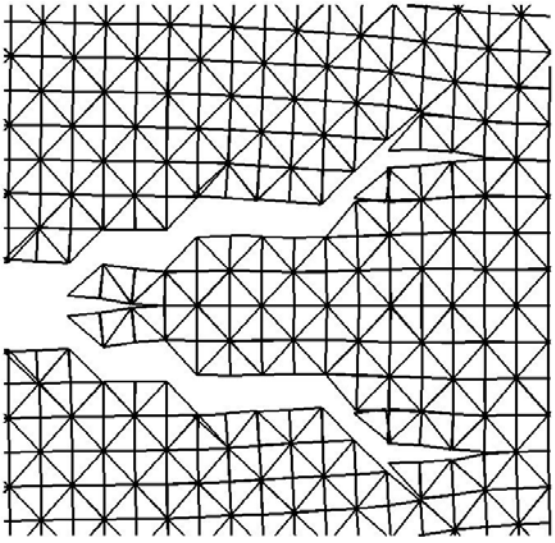

Figure 3.10. Branch jump to level-4.

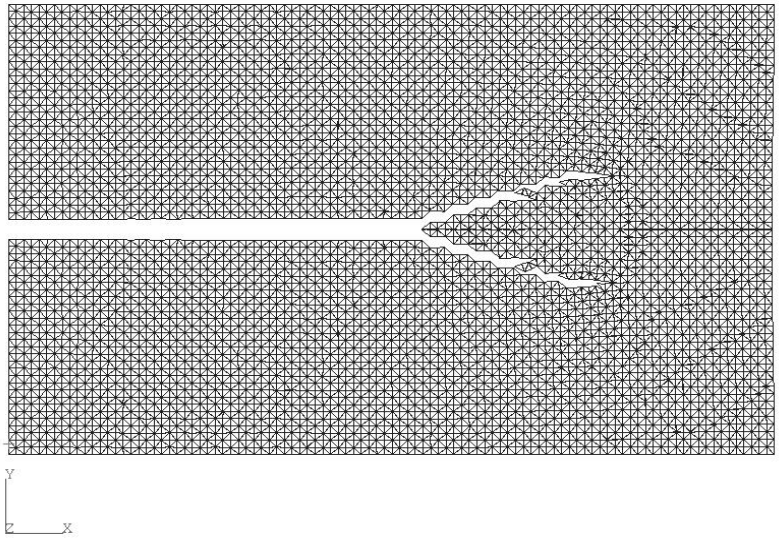

Figure 3.11. Fracture profile for $V_B$ = 5 m/s.

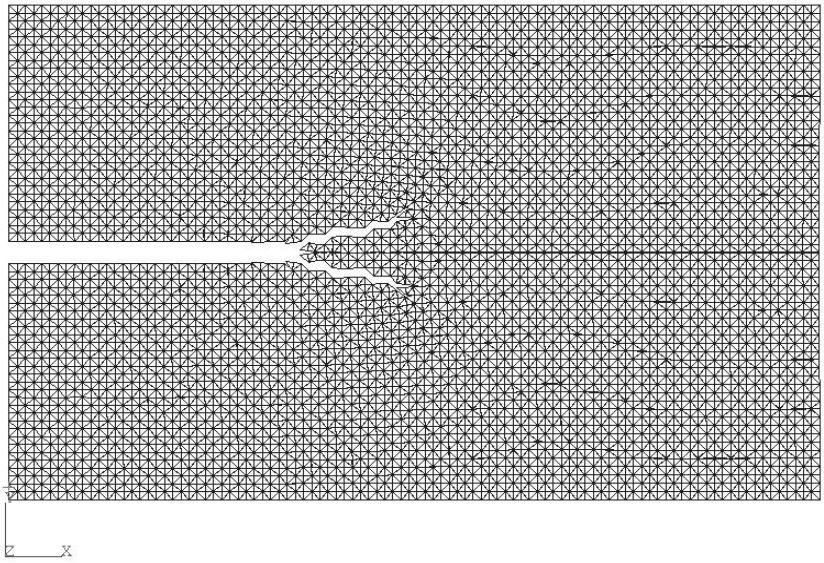

Figure 3.12. Fracture profile for $V_B$ = 10 m/s.

The final fracture profile for the two boundary cases are shown in Figure 3.11 and Figure 3.12. The angle of branching are $18^o$ for $V_B$ =5 m/s and $13^o$ $V_B$ =10 m/s, which is within the experimental range of $10^o$ to $45^o$ (Ravi-Chandar and Knauss, 1984c).

### 3.2.2. Crack Tip Velocity

The values of traction-energy slopes '$m$', which resulted in the above fracture profile for the two cases are presented in Table 3.1 and Table 3.2.

Table 3.1. Energy-traction slope values for $V_B$ = 5 m/s.

| Phase/Level | Designation | Value ($\times 10^{-3}$) |
|---|---|---|
| Phase-1 | $m_1$ | 8.40 |
| Phase-2 | $m_2$ | 24.00 |
| Phase-3 | $m_3$ | 2.40 |
| Level-1 | $m_{L1}$ | 0.24 |
| Level-2 | $m_{L2}$ | 6.00 |
| Level-3 | $m_{L3}$ | 2.80 |
| Level-4 | $m_{L4}$ | 6.72 |
| Level-5 | $m_{L5}$ | 5.4 |
| Level-6 | $m_{L6}$ | 6.00 |
| Level-7 | $m_{L7}$ | 4.20 |
| Level-8 | $m_{L8}$ | 3.60 |

Table 3.2. Energy-traction slope values for $V_B$ = 10 m/s.

| Phase/Level | Designation | Value ($\times 10^{-3}$) |
|---|---|---|
| Phase-1 | $m_1$ | 48.00 |
| Phase-2 | $m_2$ | 0.36 |
| Phase-3 | $m_3$ | 36.00 |
| Level-1 | $m_{L1}$ | 24.00 |
| Level-2 | $m_{L2}$ | 15.60 |
| Level-3 | $m_{L3}$ | 18.00 |
| Level-4 | $m_{L4}$ | 16.80 |

And the crack tip position simulated with the present model for both the case in non-dimensional units and with dimensional units is presented in Figures 3.13-3.16. In both the case, fracture initiation occurred under quasi-static conditions. After initiation, the crack tip position - in a numerically average sense – has a velocity $v=0.35c_R$ till just after initiation of branching. Immediately after branching, the crack profile is continuous, but with crack propagation the crack tip deviates from that expected for $v=0.35c_R$, i.e., the crack velocity increase. This is attributed to loss of strength of the specimen due to presence of microcracks. Also, it can be observed from the crack tip profile that the crack follows the path same as that with $v=0.75c_R$ till the activation of high inertia zone cohesive traction, $\sigma^{ir}$, at the beginning of Phase-I. On activation, the crack tip profile deviates from each other. The Phase-I (P-I in the figure), Phase-II (or P-II), Phase-III (or P-III) and branching phase are also shown in these plots.

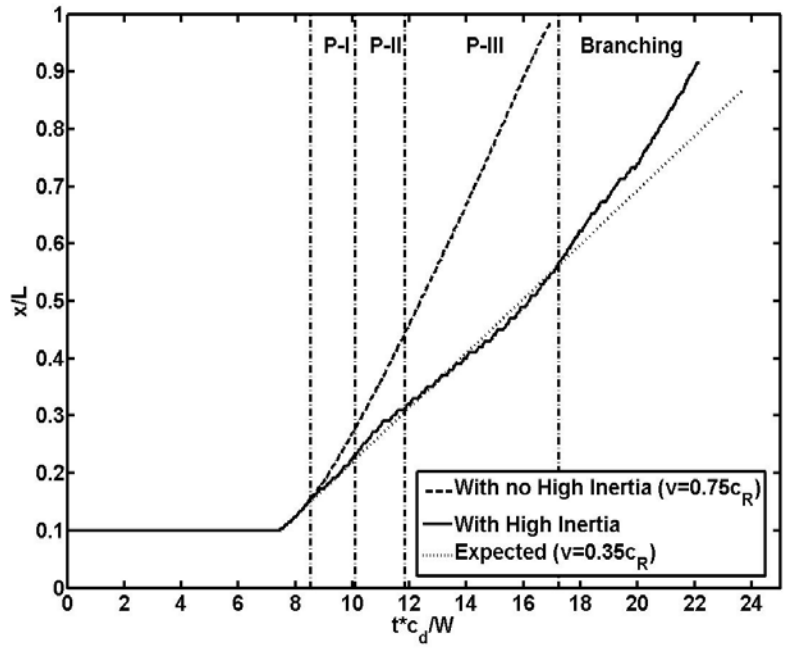


Figure 3.13. Crack tip position versus normalized time for $V_B$ = 5 m/s.

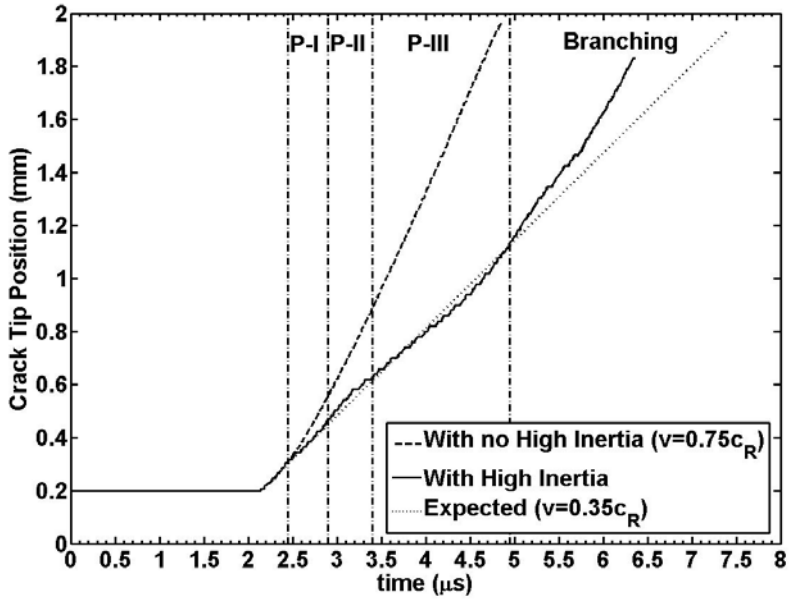


Figure 3.14. Crack tip position versus actual time for $V_B$ = 5 m/s.

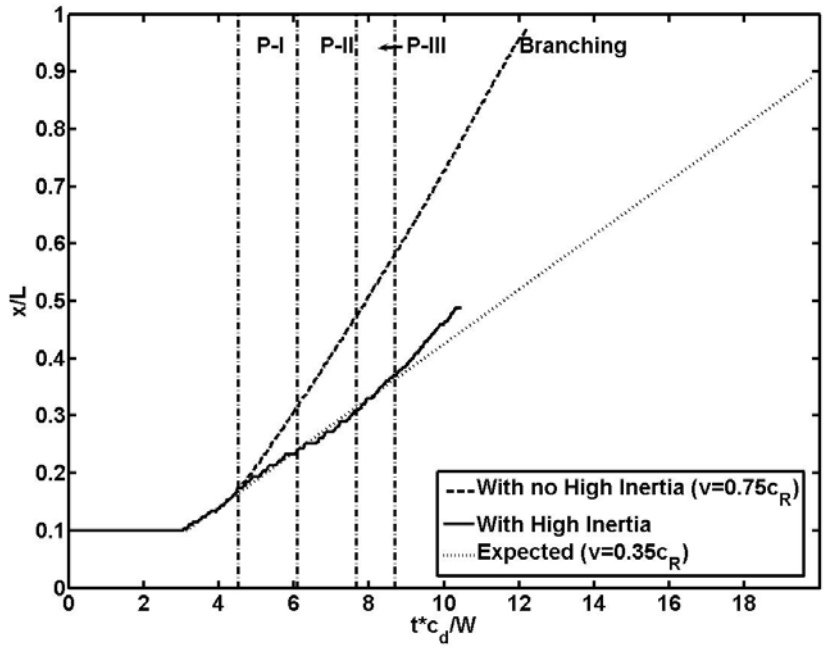


Figure 3.15. Crack tip position versus normalized time for $V_B$ = 10 m/s.

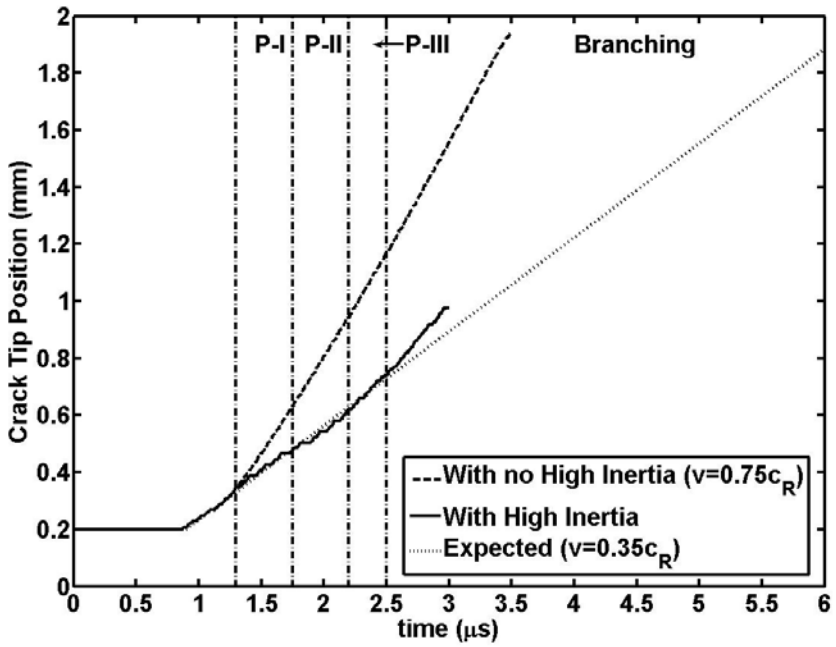


Figure 3.16. Crack tip position versus actual time for $V_B$ = 10 m/s.

The video files of the dynamic crack propagation (dcp) in each case titled ‘dcp5m_s.avi’ and ‘dcp10m_s.avi’ are attached.

### 3.2.3. Process Zone

Process zone dissipation was measured in the FEA code by calculating the accumulated stress work (ASW), $U_V$ (Freund, 1990)

$$U_V = \int_{-\infty}^{t} \int_{V} \sigma_{ji} \dot{\varepsilon}_{ij} dV dt' \tag{3.4}$$

Accumulated stress work was compared with and without the fracture dissipation term for the same position of crack tip x = 1 mm (x/L = 0.5). Numerically, the stress work is calculated and each gauss point in the element. The average value over each element is plotted. Contour plots of ASW are presented in Figure 3.17 and 3.18. As can be see from Figure 3.18 the dissipation in the case with the high inertia zone term is higher than without.

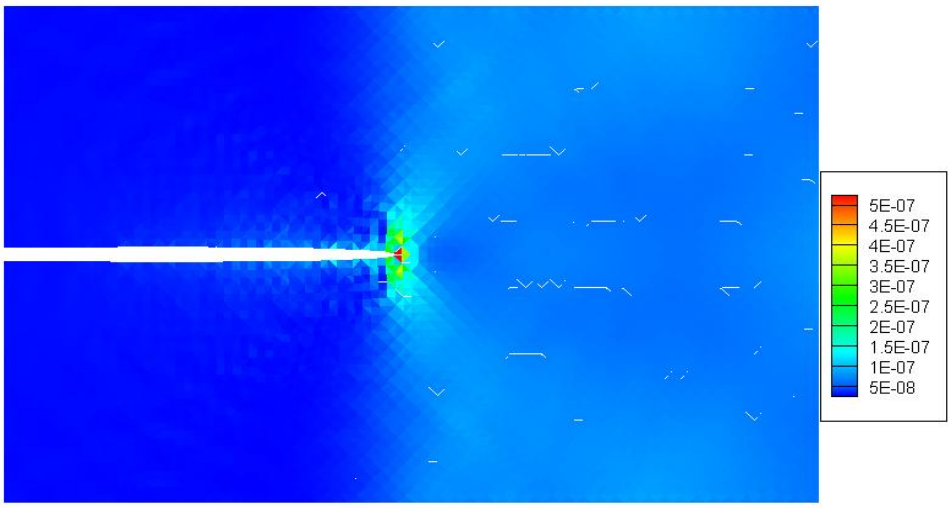


Figure 3.17. Accumulated stress work without $\sigma^{ir}$, x/L = 0.5, t = 3.5μs.

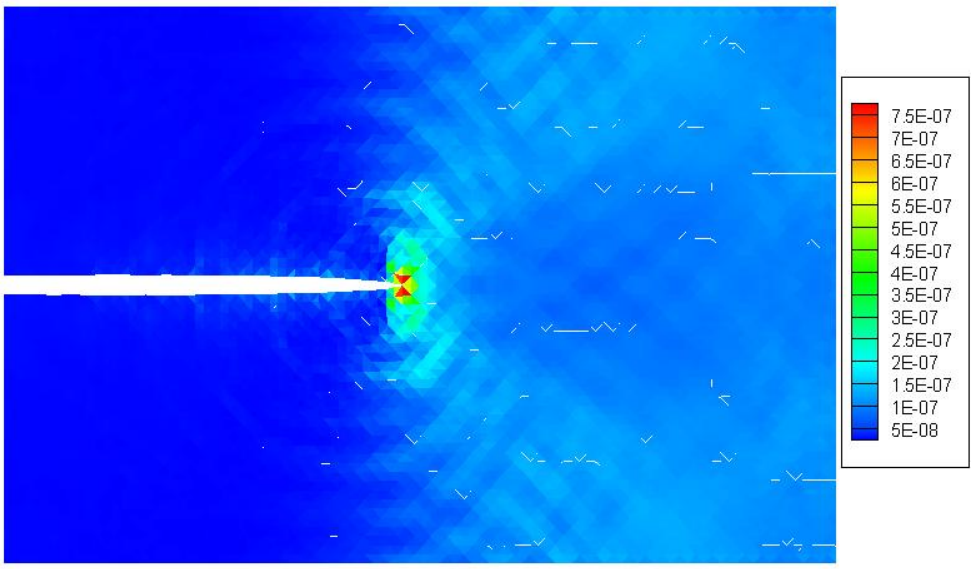


Figure 3.18. Accumulated stress work with $\sigma^{ir}$, x/L = 0.5, t = 4.5μs.

### 3.3. Non Mid-Plane Crack Problem

Qualitative behavior of non mid-plane crack as shown in Figure 3.19 is investigated with crack subjected to velocity loading of $V_B$ = 10 m/s. The material properties of PMMA presented in Table 2.3 are again used. The crack branching profile and the tip profile are for this simulation is presented in Figure 3.20 and Figure 3.21 respectively.

The propagation of crack tip away from a straight path towards the center of the specimen is due to the earlier arrival of reflected compressive waves from the base of the specimen. The slope parameters 'm' are lower than that for center crack case. Here, $m_1$ = 36 $\times 10^{-3}$, $m_2$ = 0.24 $\times 10^{-3}$ and $m_3$ = 24 $\times 10^{-3}$, indicating possible a lower energy dissipation. In other words, the center crack could possible be maximum dissipation condition. Also, initiation of each phase was earlier than that for the center crack specimen. However, these results are only qualitative in nature. Further investigations for various crack positions and different values of loading velocities are under way, but not presented.

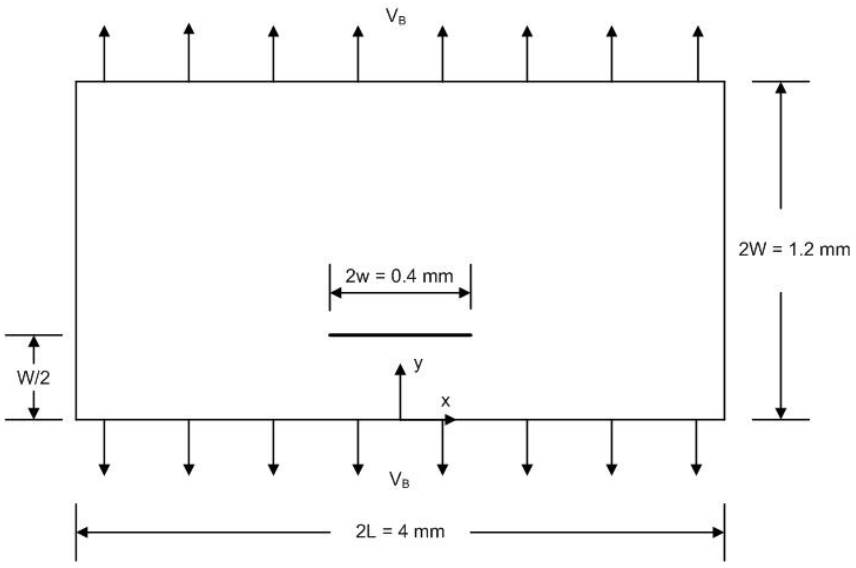


Figure 3.19. Specimen dimensions for non-mid plane crack problem.

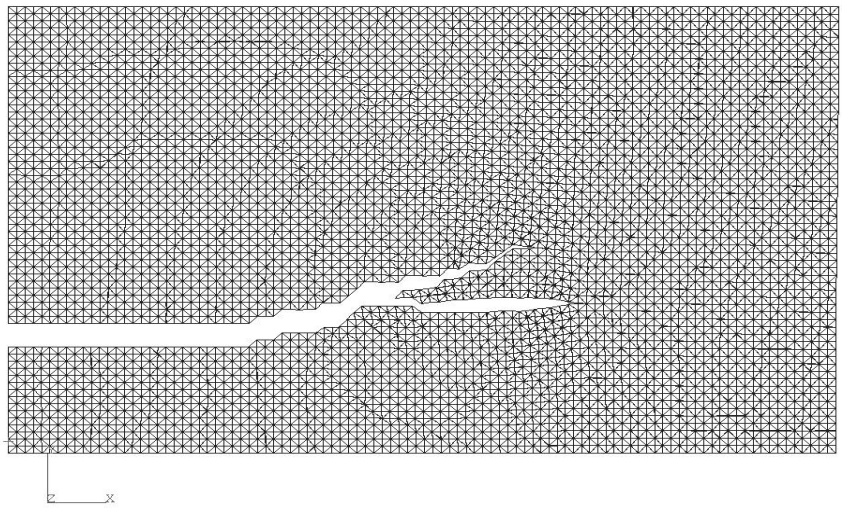

Figure 3.20. Fracture profile for non mid-plane crack.

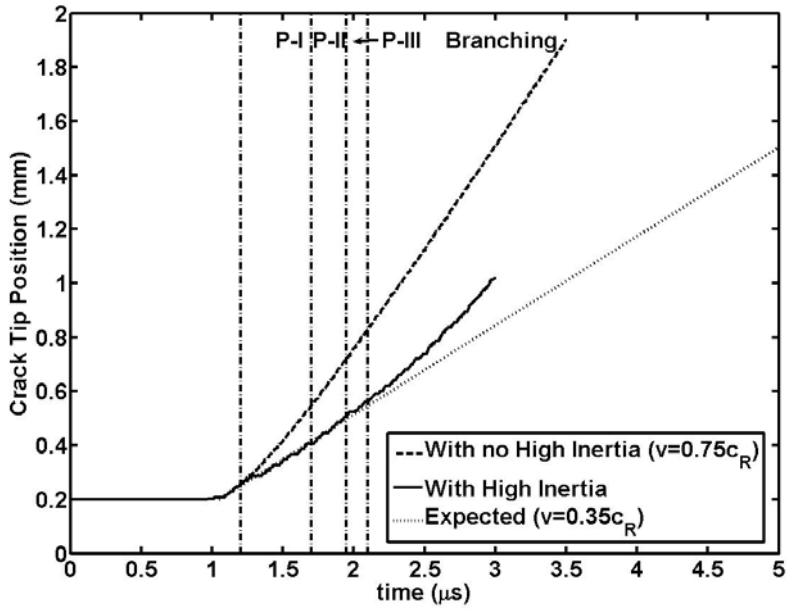


Figure 3.21. Crack tip position versus actual time for non mid-plane crack.

# 4. SUMMARY AND CONCLUSIONS

The role of microcracks and high inertia zone in dynamic brittle fracture has been critically analyzed. A nonlinear finite element code with explicit time integration scheme is developed to simulate dynamic fracture in brittle materials. An additional irreversible cohesive term is proposed and implemented in the code to model the effect of the high inertia zone.

Fracture simulation were performed for PMMA under two boundary velocity condition ($V_B$ = 5m/s and 10m/s). Crack initiated at the onset of quasi-static stress state in the specimen. Crack velocities of $0.35c_R$ were achieved. Crack propagated in three-phases before branching. Low branching angle was achieved and previous failed branch attempts were also observed in the finite element simulation. Branch angles were dependent on the choice of the new cohesive parameter 'm' introduced, hence making the problem statistical in nature.

In conclusion, dynamic brittle fracture is governed by the presence of high inertia zone very close to and ahead of the crack tip. Modeling of this zone is one of the key aspects to understand dynamic brittle fracture.

## REFERENCES

Carlsson, J., Dahlberg, L. and Nilsson, F. (1973). Experimental studies of the unstable phase of crack propagation in metals and polymers. *Dynamic Crack Propagation* (Edited by G.C. Sih), Noordhoff International Publishing, Leyden, The Netherlands, 165-181.

Costanzo, F. and Allen, D.H. (1995). A continuum thermodynamic analysis of cohesive zone models. *International Journal of Engineering Science* **15**, 2197-2219.

Costanzo, F. and Walton, J.R. (1997). A study of dynamic crack growth in elastic materials using a cohesive zone model. *International Journal of Engineering Science* **35**, 1085-1114.

Costanzo, F. (1998). A continuum theory of cohesive zone models: deformation and constitutive equation. *International Journal of Engineering Science* **36**, 1763-1792.

Costanzo, F. and Walton, J.R. (1998). Numerical simulations of a dynamically propagating crack with a nonlinear cohesive zone. *International Journal of Fracture* **91**, 373-389.

Costanzo, F. and Walton, J.R. (2002). Steady growth of a crack with a rate and temperature sensitive cohesive zone. *Journal of the Mechanics and Physics of Solids* **50**, 1649-1679.

Döll, W. (1973). An experimental study of the heat generated in the plastic region of a running crack in different polymeric materials. *Engineering Fracture Mechanics* **5**, 259-268

Doyle, M.J. (1983). A mechanism for crack branching in polymethyl methacrylate and the origins of the bands on the surfaces of fracture. *Journal of Materials Science* **18**, 687-702.

Fineberg, J., Gross, S.P., Marder, M. and Swinney, H.L. (1991). Instability in dynamic fracture. *Physical Review Letters* **67**, 457-460.

Fineberg, J., Gross, S.P., Marder, M. and Swinney, H.L. (1992). Instability in the propagation of fast cracks. *Physical Review B* **45**, 5146-5154.

Fineberg, J. and Marder, M. (1999). Instability in dynamic fracture. *Physics Reports* **313**, 1-108.

Freund L.B. (1990). *Dynamic Fracture Mechanics*. Cambridge University Press, New York.

Fuller, K.N.G., Fox, P.G. and Field, J.E. (1975). The temperature rise at the tip of fast-moving cracks in glassy polymers. *Proceedings of the Royal Society of London A* **341**, 537-557.

Gao, H. (1993). Surface roughening and branching instabilities in dynamic fracture. *Journal of the Mechanics and Physics of Solids* **41**, 457-486.

Gao, H. (1996). A theory of local limiting speed in dynamic fracture. *Journal of the Mechanics and Physics of Solids* **44**, 1453-1474.

Graff, K.F. (1975). *Wave Motion in Elastic Solids*. Ohio State University Press, Columbus.

Johnson, E. (1992). Process region changes for rapidly propagating cracks. *International Journal of Fracture* **55**, 47-63.

Kubair, D.V., Geubelle, P.H. and Huang, Y.Y. (2003). Analysis of a rate-dependent cohesive model for dynamic crack propagation. *Engineering Fracture Mechanics* **70**, 685-704.

Nishioka, T. (1997). Computational dynamic fracture mechanics. *International Journal of Fracture* **86**, 127-159.

Ravi-Chandar, K. and Knauss, W.G. (1984a). An experimental investigation into dynamic fracture – I. Crack initiation and crack arrest. *International Journal of Fracture* **25**, 247-262.

Ravi-Chandar, K. and Knauss, W.G. (1984b). An experimental investigation into dynamic fracture – II. Microstructural aspects. *International Journal of Fracture* **26**, 65-80.

Ravi-Chandar, K. and Knauss, W.G. (1984c). An experimental investigation into dynamic fracture – III. On steady-state crack propagation and crack branching. *International Journal of Fracture* **26**, 141-154.

Ravi-Chandar, K. and Knauss, W.G. (1984d). An experimental investigation into dynamic fracture – IV. On the interaction of stress waves with propagating cracks. *International Journal of Fracture* **26**, 189-200.

Ravi-Chandar, K. and Yang, B. (1997). On the role of microcracks in the dynamic fracture of brittle materials. *Journal of the Mechanics and Physics of Solids* **45,** 535-563.

Ravi-Chandar, K. (1998). Dynamic fracture of nominally brittle materials. *International Journal of Fracture* **90**, 83-102.

Reddy, J. N. (2004). *An Introduction to Nonlinear Finite Element Analysis*. Oxford University Press, New York.

Reddy, J. N. (2006). *An Introduction to the Finite Element Method*. Third Edition, McGraw-Hill, New York.

Roy, Y.A. and Dodds Jr., R.H. (2001). Simulation of ductile crack growth in thin aluminum panels using 3-D surface cohesive elements. *International Journal of Fracture* **110**, 21-45.

Washabaugh, P.D. and Knauss, W.G. (1994). A reconciliation of dynamic crack velocity and Rayleigh wave speed in isotropic brittle solids. *International Journal of Fracture* **65**, 97-114.

Xu, X.-P. and Needleman, A. (1994). Numerical simulations of fast crack growth in brittle solids. *Journal of the Mechanics and Physics of Solids* **42,** 1397-1434.

Yang, B. and Ravi-Chandar, K. (1996). On the role of the process zone in dynamic fracture. *Journal of the Mechanics and Physics of Solids* **44**, 1955-1976.

Yoffe, E. (1951). The moving Griffith crack. *Philosophical Magazine* **42**, 739-750.

Zhang, Z. (2003). Cohesive zone modeling of dynamic failure in homogeneous and functionally graded materials. M.S. Thesis, University of Illinois at Urbana-Champaign.

Zimmermann, C., Klemm, W. and Schönert, K. (1984). Dynamic energy release rate and fracture heat in polymethylmethacrylate (PMMA) and a high-strength steel. *Engineering Fracture Mechanics* **20**, 777-782.

# VITA

Name: Shankar Karedla-Ravi

Address: C/O Dr. J.N.Reddy, Department of Mechanical Engineering,
Texas A&M University, College Station, TX 77843-3123

Email Address: rskaredla@yahoo.com

Education: B.S., Naval Architecture, Indian Institute of Technology-Madras, 1999
M.S., Mechanical Engineering, University of Missouri-Rolla, 2001
Ph.D., Mechanical Engineering, Texas A&M University, 2006